UNIVERSITY OF ZAGREB
FACULTY OF MECHANICAL ENGINEERING AND NAVAL ARCHITECTURE

MASTER'S THESIS

Marija Stipić

Zagreb, 2019.

UNIVERSITY OF ZAGREB
FACULTY OF MECHANICAL ENGINEERING AND NAVAL ARCHITECTURE

NUMERICAL MODELLING OF COMBUSTION PROCESS USING FLAMELET GENERATED MANIFOLD AND COHERENT FLAME COMBUSTION MODEL

Supervisor:
Asst. Prof. Milan Vujanović, PhD

Student:
Marija Stipić

Zagreb, 2019.

SVEUČILIŠTE U ZAGREBU
FAKULTET STROJARSTVA I BRODOGRADNJE
Središnje povjerenstvo za završne i diplomske ispite
Povjerenstvo za diplomske ispite studija strojarstva za smjerove:
procesno-energetski, konstrukcijski, brodostrojarski i inženjersko modeliranje i računalne simulacije

Sveučilište u Zagrebu Fakultet strojarstva i brodogradnje	
Datum	Prilog
Klasa:	
Ur. broj:	

DIPLOMSKI ZADATAK

Student: **Marija Stipić** Mat. br.: 0035200512

Naslov rada na hrvatskom jeziku: **Numeričko modeliranje procesa izgaranja pomoću tabeliranih podataka propagacije plamena i modela izgaranja koherentnih plamenova**

Naslov rada na engleskom jeziku: **Numerical Modelling of Combustion Process Using Flamelet Generated Manifold and Coherent Flame Combustion Models**

Opis zadatka:

Korištenje računalne dinamike fluida (RDF) u kombinaciji s eksperimentalnim istraživanjem postao je uobičajen pristup u razvoju motora s unutarnjim izgaranjem. U dizelskim motorima porast temperature plina u komori izgaranja prilikom kompresijskog takta uzrokuje zapaljenje smjese isparenog goriva i zraka. Numeričko modeliranje procesa izgaranja goriva može se opisati pomoću dva pristupa: detaljne kemijske kinetike i modela izgaranja. Numeričko rješavanje detaljne kemijske kinetike računalno je iznimno zahtjevno, jer je za svaku kemijsku vrstu potrebno riješiti dodatnu transportnu jednadžbu. Zbog toga u ovom radu potrebno je proces izgaranja računati metodom tabeliranja kemijskih vrsta u pretprocesoru, jer nam takav pristup omogućava efikasno numeričko rješavanje procesa izgaranja bez ograničenja što se tiče složenosti kemijske kinetike ili dostupnih računalnih resursa. Podatke o masenim udjelima kemijskih vrsta tijekom RDF procedure potrebno je dobiti interpolacijom iz izračunatih tablica u pretprocesoru. Rezultate procesa izgaranja dobivene pomoću tabeliranih podataka propagacije plamena potrebno je usporediti s eksperimentom i modelom koherentnih plamenova, koji je konvencionalni model izgaranja u motorima s unutarnjim izgaranjem.

U okviru diplomskog rada potrebno je:
1. Opisati osnovne jednadžbe računalne dinamike fluida te opisati jednadžbe modeliranja kemijske kinetike pomoću pristupa tabeliranih podataka propagacije plamena i jednadžbe modela izgaranja;
2. Prikazati numeričke metode korištene za rješavanje zadatka;
3. Korištenjem komercijalnog programskog paketa „AVL FIRE™ Workflow Manager" napraviti detaljnu numeričku simulaciju na pomičnoj mreži industrijskog dizel motora;
4. Analizirati i usporediti dobivene rezultate s dostupnim eksperimentalnim podacima.

Sva potrebna literatura za opis modela te eksperimentalni, ulazni i početni podaci za analizu bit će dostupni od strane mentora i neposrednog voditelja.

U diplomskom radu potrebno je navesti svu korištenu literaturu i eventualnu pomoć pri izradi rada.

Zadatak zadan:	Datum predaje rada:	Predviđeni datum obrane:
26. rujna 2019.	28. studenoga 2019.	2. – 6. prosinca 2019.

Zadatak zadao:

Doc. dr. sc. Milan Vujanović

Predsjednica Povjerenstva:

Prof. dr. sc. Tanja Jurčević Lulić

Foremost, I express my sincere gratitude to my supervisor, Professor Milan Vujanović, for an incredible opportunity to learn and work in his team.

I would like to express my deepest gratitude to Filip Jurić as his interest, will and ability to help were tireless. Without his knowledge, guidance and help this thesis would not have reached its present quality. I am especially grateful for his everyday unselfish support and encouragement.

I would also like to thank the rest of the PowerLab CFD team, Ivan Pađen, Tibor Bešenić and Marko Ban, for encouraging me and making the time I spent there both interesting and fun.

Special thanks to my dear friends, Blaženka and Kristina, for making my student time worth remembering.

Last, but not least, I would like to thank my parents and my brothers, especially Matej, for their understanding, patience and great support through my entire education.

Statement / Izjava

I hereby declare that I have made this thisis independently using the knowledge acquired during my studies and the cited references.

Izjavljujem da sam ovaj rad izradila samostalno koristeći znanja stečena tijekom studija i navedenu literaturu.

Zagreb, 2019 Marija Stipić

Contents

List of Figures

List of Tables

List of Symbols

Latin	**Description**	**Unit**
A	Coefficient in Arrhenius law	
c	Progress variable	
c_{var}	Progress variable variance	
c_p	Specific heat capacity	$J\ kg^{-1}K^{-1}$
C_D	Drag coefficient	
C_1	WAVE breakup model constant 1	
C_2	WAVE breakup model constant 2	
C_μ	$k-\zeta-f$ turbulence model constant	
d	Droplet diameter	m
D	Effective diffusion coefficient	$m^2\ s^{-1}$
D_{ij}	Rate of deformation tensor	$N\ m^{-2}$
E_β	Activation energy	$J\ kg^{-1}$
E_1	Abramzon-Sirignano model constant 1	
E_2	Abramzon-Sirignano model constant 2	
e	Specific total energy	$J\ kg^{-1}$
f	Elliptic function	
f	Mixture fraction	
f_i	Volume forces	N
F	Force	N
F_d	Drag force	N
g_i	Cartesian component of the force vector	$m\ s^{-2}$
g	Residual gas mass	
h	Enthalpy	$kJ\ kg^{-1}$
k	Turbulent kinetic energy	$m^2\ s^{-2}$
k_i	Reaction rate coefficient	
L	Turbulent length	
l	Length of the nozzle	m

m	Total mass	kg
m_i	Mass of species i	kg
m_p	Parcel mass	kg
P_k	Production of turbulent kinetic energy	W
p	Pressure	Pa
q	Heat flux	W m^{-2}
r	Droplet radius	m
R	Ideal gas constant	J $(mol\ K)^{-1}$
S_φ	Source of extensive property	
t	Time	s
T	Temperature	K
u,v	Velocity	m s^{-1}
V	Volume	m^3
W	Molecular weight of species k	kg $kmol^{-1}$
x	Cartesian coordinates	m
Y	Mass fraction	
Z	Mixture fraction	
Z_{var}	Mixture fraction variance	

Greek	**Description**	**Unit**
α	Volume fraction	
β	Coefficient in Arrhenius law	
β_g	Binary diffusion coefficient	
γ	Half outer cone angle	rad
δ_{ji}	Kronecker delta	
ε	Turbulent kinetic energy dissipation rate	$m^2\ s^{-3}$
Γ	Diffusion coefficient	
λ	Thermal conductivity coefficient	W $m^{-1}K^{-1}$
λ_w	Wavelength	m
μ	Molecular viscosity	N $m^{-2}s^{-1}$
$\sum$	Flame surface density	
ζ	Velocity scale ratio	
ρ	Density	kg m^{-3}

σ_{ji}	Surface forces	N
τ_a	Breakup time	s
τ_{ji}	Viscous stress tensor	N m^{-2}
φ	Extensive property of general conservation equation	
ω	Reaction rate	
χ	Scalar dissipation rate	
Ω	Wave growth rate	s

Abbreviations	**Description**	-
BDC	Bottom dead center	
CA	Crank angle	
CDS	Central differencing scheme	
CFD	Computational fluid dynamics	
CMD	Continuous droplet model	
DDM	Dispersed droplet model	
DNS	Direct numerical simulation	
ECFM	Extended coherent flame model	
ECFM-3Z	Three-zones extended coherent flame model	
EGR	Exhaust gas recirculation	
FGM	Flamelet generated manifold	
GDI	Gasoline direct injection	
HCCI	Homogeneous charge compression ignition	
HCN	Hydrogen cyanide	
IC	Internal combustion	
LES	Large eddy simulation	
PDF	Probability density function	
PSR	Perfectly stirred reactor	
PM	Particulate matter	
RANS	Reynolds averaged Navier-Stokes equations	
RoHR	Rate of heat release	
TDC	Top dead center	

Other Symbols

Nu	Nusselt number
Oh	Ohnesorge number
Re	Reynolds number
Pr	Prandtl number
Sc	Schmidt number
Se	Sherwood number
We	Weber number

Sažetak

Korištenje računalne dinamike fluida (RDF) u kombinaciji s eksperimentalnim istraživanjima je postao nezaobilazan pristup u razvoju dizel motora. Proces izgaranja je vrlo kompleksan fenomen, a numerički se može opisati pomoću dva pristupa: detaljne kemijske kinetike i modela izgaranja. Detaljna kemijska kinetika pruža opsežan uvid u kemijske aspekte procesa izgaranja, dok su modeli izgaranja opisani s aproksimiranom kemijskom kinetikom s ciljem smanjenja potrebe za računalnim resursima. Pristup u modeliranju izgaranja koji omogućava efikasno numeričko rješavanje procesa izgaranja bez ograničenja na složenost kemijske kinetike ili dostupnih računalnih resursa je metoda tabeliranja kemijskih vrsta u predprocesoru (engl. Flamelet generated manifold, FGM). Ovim pristupom detaljna kemijska kinetika se izračunava u predprocesoru, a rezultati se spremaju u tablicu koja se interpolira tijekom RDF procedura. Jedan od konvencionalnih modela izgaranja u motorima s unutarnjim izgaranjem je model koherentnih plamenova (engl. Three-zones extended coherent flame model, ECFM-3Z+). U ovom radu za modeliranje procesa izgaranja u dizel motoru korišten je FGM pristup i ECFM-3Z+ model. Cilj ovog rada je analizirati i validirati rezultate numeričkih simulacija s eksperimentalnim podacima. Numeričke simulacije izvršene su korištenjem komercijalnog programskog paketa AVL FIRE^{TM}. Rezultati poput tlaka, temperature, brzine oslobađanja topline i NO emisija izračunati su za radne točke motora s jednim i s tri ubrizgavanja goriva u cilindar. Trend emisija NO-a izmjeren u eksperimentu dobro je reproduciran s oba modela. Budući da se rezultati oba korištena pristupa u modeliranju izgaranja dobro poklapaju s eksperimentalnim podacima, zaključeno je da su i ECFM-3Z+ model i FGM pristup valjani za opisivanje procesa izgaranja u industrijskim dizel motorima.

Ključne riječi: Modeliranje izgaranja, Tabelacija, Dizel motor, NO emisije

Abstract

In recent times, combustion modelling employing computational fluid dynamics (CFD) in combination with experiment has become an irreplaceable tool in the design process of the diesel engines. Combustion process as a phenomenon of exceptional complexity can be numerically solved with detailed chemical kinetics or with the utilisation of approximated combustion models. Detailed chemical kinetics provides a comprehensive insight into the chemical aspect of the combustion process, while combustion models are described with approximated chemical kinetics in order to reduce the computational demand. An appropriate modelling approach to overcome these challenges is the Flamelet generated manifold (FGM) combustion modelling approach, which computes the chemistry kinetics in preprocessing and stores the result data in a look-up table that is interpolated during the CFD simulations. One of the combustion models, which has proven an ability to simulate the combustion process in internal combustion engines is Three-zones extended coherent flame model (ECFM-3Z+). In this thesis, ECFM-3Z+ and FGM approaches were employed for the calculation of combustion process in a diesel engine. The primary aim of the thesis is to analyse and validate numerical results obtained with FGM and ECFM-3Z+ models against experimental data. Numerical simulations are performed using commercial CFD software AVL FIRE^{TM}, where the calculated results such as mean in-cylinder pressure, mean temperature, rate of heat release and NO emissions are calculated for single and multi-injection strategies. The NO emission trend observed in the experiment is well reproduced with both combustion models, while the computational time for CFD simulations with FGM is reduced by half. The results obtained with both combustion modelling approaches are found to be in a good agreement with the experimental data. Thus it is conducted, that both ECFM-3Z+ and FGM combustion modelling approaches are capable of predicting the combustion process in the real industrial diesel engines.

Keywords: Combustion modelling, Tabulation, Diesel engine, NO Emissions

Prošireni sažetak

Korištenje računalne dinamike fluida (RDF) u kombinaciji s eksperimentalnim istraživanjima je postao nezaobilazan pristup u razvoju motora s unutarnjim izgaranjem budući da omogućava bolje razumijevanje procesa izgaranja. U svrhu što boljeg simuliranja procesa izgranja potrebno je obuhvatiti kemijske i fizikalne fenomene koji se događaju prilikom izgaranja. Dva pristupa za rješavanje kemijskih procesa izgaranja RDF-om su korištenje modela izgaranja ili rješavanje kemijske kinetike. Većina modela izgranja koristi osnovni skup kemijskih jednadžbi koji pruža zadovoljavajuće rezultate kada nije potreban detaljan uvid u proces izgaranja, dok je za detaljniji opis izgaranja potrebno koristiti detaljnu kemijsku kinetiku što rezultira s većom potrebom za računalnim resursima. Stoga novi pristupi u modeliranju izgaranja koriste postupak tabelacije kemijskih vrsta u pred-procesiranju koji omogućava korištenje detaljne kemijske kinetike s prihvatljivom potrebom za računalnim resursima. Cilj ovoga rada je analizirati i usporediti rezultate numeričkih simulacija dobivenih korištenjem dva različita pritupa modeliranja izgaranja.

Matematički model

Svi zakoni očuvanja proizvoljnog fizikalnog svojstva kojima se rješavaju problemi u računalnoj dinamici fluida predstavljaju specijalizirani oblik opće transportne jednadžbe:

$$\frac{\partial}{\partial t}(\rho\varphi) + \frac{\partial}{\partial x_j}(\rho\varphi u_j) = \frac{\partial}{\partial x_j}\left(\Gamma_\varphi \frac{\partial \varphi}{\partial x_j}\right) + S_\varphi \tag{0.1}$$

gdje prvi član lijeve strane jednadžbe predstavlja brzinu promjene fizikalnog svojstva, a drugi konvekcijski tok. Nadalje, prvi član s desne strane jednadžbe predstavlja difuziju, dok drugi predstavlja izvor ili ponor fizikalnog svojstva φ. Zamjenom općenite vrijednosti φ s fizikalnom veličinom gustoće ρ, količinom gibanja ρu ili energijom ρe dobivaju se osnovne jednadžbe koje opisuju strujanje fluida:

- Zakon očuvanja mase

$$\frac{\partial \rho}{\partial t} + \frac{\partial}{\partial x_j}(\rho u_j) = 0 \tag{0.2}$$

- Zakon očuvanja količine gibanja

$$\frac{\partial}{\partial t}(\rho u_i) + \frac{\partial}{\partial x_j}(\rho u_j u_i) = \rho f_i + \frac{\partial \sigma_{ji}}{\partial x_j} \tag{0.3}$$

- Zakon očuvanja energije

$$\frac{\partial}{\partial t}(\rho e) + \frac{\partial}{\partial x_j}(\rho u_j e) = \rho g_i u_i + \frac{\partial}{\partial x_j}(\sigma_{ji} u_i) - \frac{\partial q_i}{\partial x_i} + S_v \tag{0.4}$$

Osim za strujanje fluida, opća transportna jednadžba vrijedi i za očuvanje mase kemijskih vrsta, gdje izvorski/ponorski član predstavlja kemijske reakcije stvaranja i nestajanja kemijskih vrsta.

Modeliranje turbulencije

Strujanje fluida može biti laminarno, prijelazno ili turbulentno, no gotovo sva strujanja u inženjerskoj praksi su turbulentna. Turbulencija je nestacionarna, nelinearna, stohastična i trodimenzionalna pojava kod strujanja fluida pri visokim vrijednostima Reynoldsovog broja. Pojava turbulencije značajno otežava rješavanje jednadžbi strujanja fluida stoga se turbulencija najčešće modelira korištenjem Reynoldsovog osrednjavanja Navier-Stokesovih jednadžbi. Ovaj pristup pretpostavlja da sve vrijednosti u domeni (polje brzine, tlaka i sl.) variraju oko srednje vrijednosti. U ovom radu korišten je $k - \zeta - f$ model turbulencije koji je podržan u programskom paketu AVL FIRE™ [15].

Modeliranje spreja

Učinkovito izgaranje tekućih goriva i emisije štetnih dimnih plinova ovise o procesu miješanja goriva i zraka, a na taj proces jako utječe dinamika spreja. U ovom radu za modeliranje procesa spreja korišten je Euler Lagrangeov pristup diskretnih kapljica u kojem se kapljevito gorivo grupira u skupine kapljica (parcele) sličnog promjera i sličnih fizikalnih svojstava. Za svaku parcelu računa se njihova trajektorija i rješavaju Lagrangeove jednadžbe očuvanja u odnosu na plinovitu fazu koja se tretira kao kontinuum. Sila koja ima najveći utjecaj na gibanje parcele je sila otpora. Trajektorija i brzina kapljice izvodi se iz drugog Newtonovog zakona:

$$m_p \frac{du_{id}}{dt} = \sum F_i \,, \tag{0.5}$$

pri čemu je m_p masa parcele, a $\sum F_i$ suma svih sila koje djeluju na tu parcelu.

Kako bi se točnije opisao proces spreja, koriste se određeni modeli poput isparavanja, sudaranja, spajanja, deformacije kapljica, turbulentne disperzije te primarnog i sekundarnog raspadanja kapljica.

Za modeliranje raspadanja kapljica korišten je Wave model. Zbog nestabilnih površinskih valova, nastalih uslijed izražene relativne brzine između kapljice goriva i struje zraka, dolazi do odvajanja mase i kreiranja novih kapljica manjeg promjera. Brzina raspadanja kapljice, odnosno brzina smanjenja radijusa, dana je izrazom [32]:

$$\frac{dr}{dt} = -\frac{(r - r_{stable})}{\tau_a}, \tag{0.6}$$

gdje r_{stable} predstavlja radijus kapljice nakon raspada, a τ_a vrijeme raspada. Veza između radijusa novonastale kapljice, r_{stable} i najbrže rastućeg vala glasi:

$$r_{stable} = A \cdot C_1 \,. \tag{0.7}$$

Osim raspadanja korišten je i Abramzon-Sirignano model isparavanja, temeljen na klasičnoj teoriji filma. Pretpostavka modela je jednolika raspodjela temperature po promjeru kapljice te njezina sferična geometrija [34].

Modeliranje izgaranja

Numeričko modeliranje procesa izgaranja goriva može se opisati korištenjem detaljne kemijske kinetike ili modela izgaranja. Pristup kemijske kinetike daje detaljan uvid u kemijske procese tijekom izgaranja. Međutim, takav pristup je iznimno računalno zahtjevan budući da je potrebno rješavanje transportne jednadžbe za svaku kemijsku vrstu u reakcijskom mehanizmu [5]. To je dovelo do razvoja različitih modela izgaranja kojima se nastoji ubrzati proces računanja. U ovom radu, proces izgaranja goriva modeliran je korištenjem dva različita pristupa:

1.) Model izgaranja
2.) Pristup tabeliranih podataka propagacije plamena

Model izgaranja korišten u ovom radu, naziva se prošireni model koherentnih plamenova (engl. Three-zones extended coherent flame model), u daljnjem tekstu ECFM-3Z+. Ovaj model uz osnove jednadžbe mehanike fluida rješava dodatne transportne jednadžbe unutar tri zone

miješanja za slijedeće kemijske vrste: gorivo, $O_2, N_2, H_2, CO_2, CO, H_2O, H, N, O, OH$ i NO [2].

Pristup tabeliranih podataka propagacije plamena (engl. Flamelet generated manifold, FGM) omogućava numeričko rješavanje procesa izgaranja korištenjem detaljne kemijske kinetike uz značajno smanjenje trajanja simulacija [20]. Ovo je omogućeno rješavanjem kemijskog mehanizma u pred-procesiranju te spremanjem nužnih i željenih određenih svojstava plamena u tabličnom obliku. Podaci koji se nalaze u tablici:

- tlak,
- temperatura,
- omjer miješanja,
- varijabla napredovanja reakcija,
- udio zastalih dimnih plinova,
- parametar sastava goriva,

interpoliraju se tijekom same RDF procedure. Maseni udjeli pojednih kemijskih vrsta funkcija su dvaju skalara: omjera miješanja i varijable napredovanja reakcija. Omjer miješanja je veličina koja određuje smjesu goriva i zraka, a varijabla napredovanja reakcija opisuje tijek izgaranja od stanja svježe smjese do izgorenog plina. Tijekom numeričke simulacije izgaranja osim osnovnih jednadžbi mehanike fluida rješavaju se transportne jednadžbe za omjer miješanja i varijablu napredovanja reakcija te njihove varijance.

Modeliranje štetnih emisija

Izgaranjem dizelskih goriva emitiraju se značajne količine dušikovih oksida (NO_x) u atmosferu. Dušikovi oksidi su naziv koji obuhvaća sedam štetnih dušikovih spojeva: $NO, NO_2, N_2O, N_2O_2, N_2O_3, N_2O_4\ i\ N_2O_5$. Izgaranjem dizelskih goriva dominantno nastaje dušikov oksid (NO) dok su koncentracije ostalih kemijskih vrsta zanemarive [39]. Stoga, su u ovom radu sve emisije NO_x-a modelirane kao NO. Za modeliranje NO-a korišten je prošireni Zeldovich model pomoću kojeg se modelira stvaranje termalnog NO-a. Kako bi se što točnije modelirao proces nastajanja NO-a u obzir je uzet i promptni mehanizam nastajanja NO-a.

Numeričke postavke

Eksperimentalni podaci dobiveni su strane od AVL-a. Glavne karakteristike eksperimentalnog diezel motora prikazane su u Tablica 1.

Tablica 1. Karakteristike eksperimentalnog motora

Tip motora	4-taktni DI diezel motor
Model	Volvo I5D
Broj cilindra	5, redni
Volumen (cm^3)	2400
Promjer (mm)	81
Stapaj (mm)	93.15
Kompresijski omjer	15.6

Numeričke simulacije izvršene su korištenjem komercijalnog programskog paketa AVL FIRE^{TM}. Generirane su tri računalne domene kako bi se ispitao utjecaj mreže na rezultate numeričke simulacije. Za daljnje računanje procesa izgaranja goriva korištena je mreža s najmanjim brojem kontrolnih volumena, budući da pruža kraće vrijeme računanja i zadovoljavajuću točnosti rezultata u usporedbi s mrežama koje sadrže više kontrolnih volumena. Zadani rubni uvjeti numeričke simulacije prikazani su u Tablica 2, dok su korišteni početni uvjeti prikazani u Tablica 3. Pri čemu Slučaj 1 i Slučaj 2 predstavljaju radne točke s jednim ubrizgavanjem goriva u cilindar motora, dok su Slučaj 3 i Slučaj 4 radne točke s tri ubrizgavanja. Osim definiranja inicijalnog tlaka i temperature, prilikom simuliranja procesa izgranja potrebno je odrediti i početni sastav plina koji se nalazi unutar računalne domene na početku simulacije. Na Slika 1 je prikazana mreža s pripadajućim definiranim selekcijama. Mreža je generirana samo za jednu sedminu geometrije budući da sapnica ima sedam rupa za ubrizgavanje goriva.

Tablica 2. Rubni uvjeti

Selekcija	Rubni uvjet	Specifičnost uvjeta
Klip	Pomična mreža	Temperatura 473 K
Segment	Cirkulacija ulaz/izlaz	Cirkulacija
Glava cilindra	Zid	Temperatura 443 K
Komp. volumen	Pomična mreža/zid	Adijabatski (0 W/m^2)
Os cilindra	Simetrija	-
Stijenka cilindra	Zid	Temperatura 423 K

Tablica 3. Početni uvjeti

	Slučaj 1	Slučaj 2	Slučaj 3	Slučaj 4
Tlak (Pa)	219284	228547	210867	218474
Teemperatura (K)	427.2	388.6	418.9	365.4
Turbulentna skala (m)	0.002	0.002	0.002	0.002
Turbulentna kinetička energija (m^2/s^2)	10	10	10	10

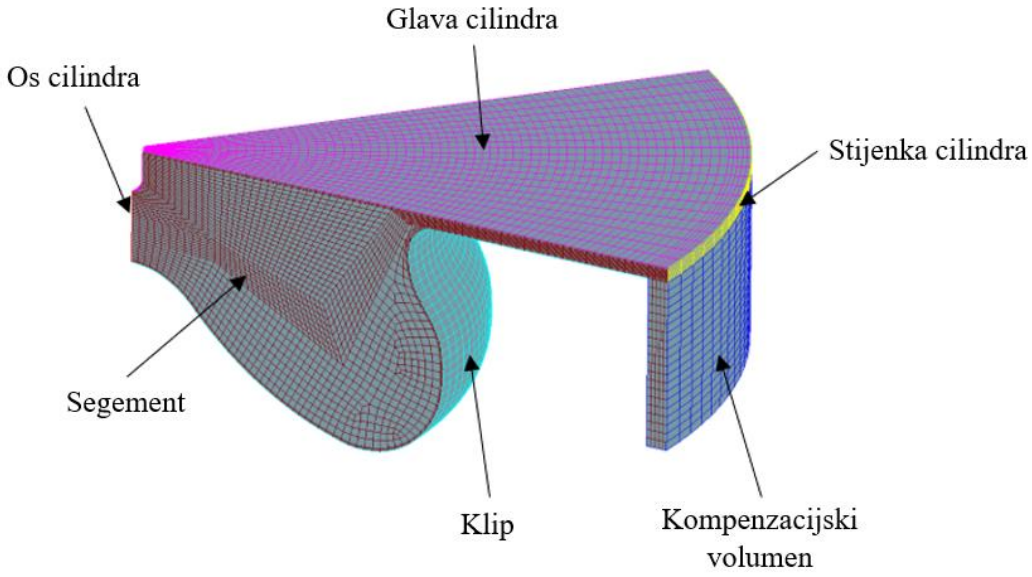

Slika 1. Mreža s definiranim selekcijama za rubne uvjete

Postavke spreja

Podaci o bizgaljci potrebni za modeliranje procesa spreja prikazani su u Tablica 4. U ovom radu korišteno je dizelsko gorivo prema normi EN590 B7 čija su svojstva implementirana u programski paket AVL FIRE^{TM}. Temperatura ubrizgavanog goriva mjerena je tijekom eksperimenta te iznosi 317.1 K. Konstante Abramzon-Sirignano modela E_1 i E_2, te konstanta Wave modela C_2 zadane su za svaku radnu točku posebno. Nadalje, različite konstante korištene su prilikom simuliranja procesa izgaranja s ECFM-3Z+ i FGM modelom. Detaljniji opis postavka numeričkih simulacija nalazi se u glavnom dijelu rada.

Tablica 4. Karakteristike brizgaljke

Pozicija	(0.5, 0, -1.5) mm
Smjer	(0, 0, 1)
Kut između osi spreja	145°
Promjer sapnice	1.84 mm
Promjer otvora sapnice	0.125 mm

Rezultati

Po završetku simulacija provedena je analiza i validacija dobivenih rezultata s dostupnim eksperimentalnim podacima. Prikazani su rezultati za po volumenu prosječnog tlaka, temperature i brzine oslobađanja topline u cilindru za radne točke s jednim ubrizgavanjem i s tri ubrizgavanja goriva u cilindar motora. Nadalje, emisije NO-a izračunate numeričkim simulacijama uspoređene su s emisijama izmjerenima u ispušnoj cijevi motora tijekom provođenja eksperimenata. Na kraju je uspoređeno vrijeme potrebno za računanje procesa izgaranja korištenjem FGM pristupa s vremenom trajanja simulacije u kojoj se koristi ECFM-3Z+ model.

Rezultati po volumenu prosječnog tlaka za radnu točku s jednim ubrizgavanjem prikazani su na Slika 2. Oba modela izagaranja pokazuju gotovo savršeno podudaranje s eksperimentalnom krivuljom u procesu kompresije i ekspanzije. Do odstupanja od eksperimentalne krivulje dolazi nakon samozapaljenja, pri čemu FGM simulacija rezultira sa značajno nižim vršnim tlakom od eksperimentalnog, dok ECFM-3Z+ simulacija izvrsno

predviđa vršni tlak. Slika 3 prikazani su rezultati po volumenu prosječne temperature. Vidljivo je da oba modela izgaranja dobro predviđaju oblik eksperimentalne krivulje. Iako, FGM simulacija pokazuje bolje predviđanje vršne temperature, te bolje slaganje s eksperimentalnim podacima u fazi ekspanzije u usporedbi s ECFM-3Z+ simulacijom. Slika 4 prikazuje usporedbu krivulje brzine oslobađanja topline dobivene korištenjem ECFM-3Z+ modela i FGM pristupa s eksperimentalno dobivenom krivuljom. Iz prikazanih rezultata vidljivo je da ECFM-3Z+ model predviđa nešto ranije zapaljenje smjese goriva i zraka u usporedbi s rezultatima dobivenima korištenjem FGM pristupa. Nadalje, može se primjetiti da krivulja dobivena korištenjem FGM pristupa ima veći gradijent nakon zapaljenja te izraženiju lokalnu maksimalnu vrijednost u odnosnu na krivulju dobivenu korištenjem ECFM-3Z+ modela.

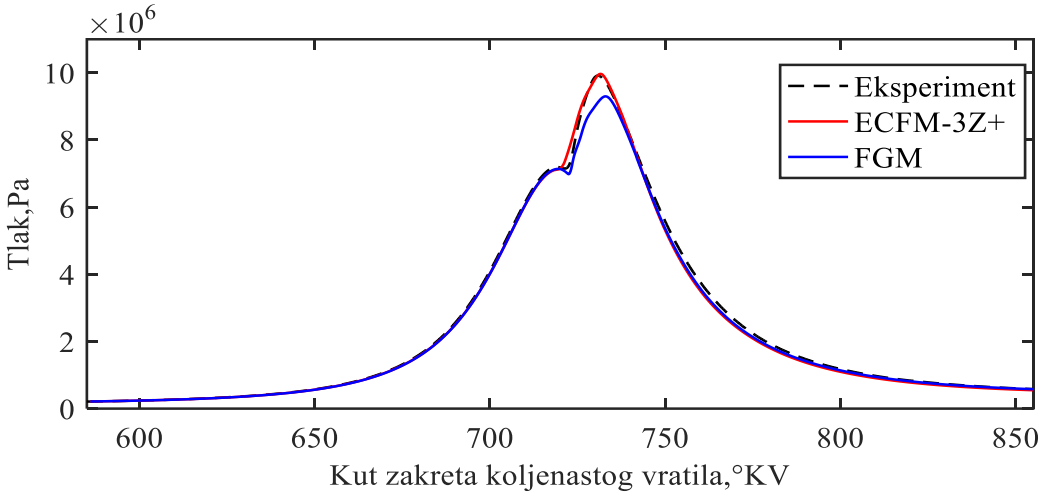

Slika 2. Usporedba po volumenu prosječnog tlaka za Slučaj 1

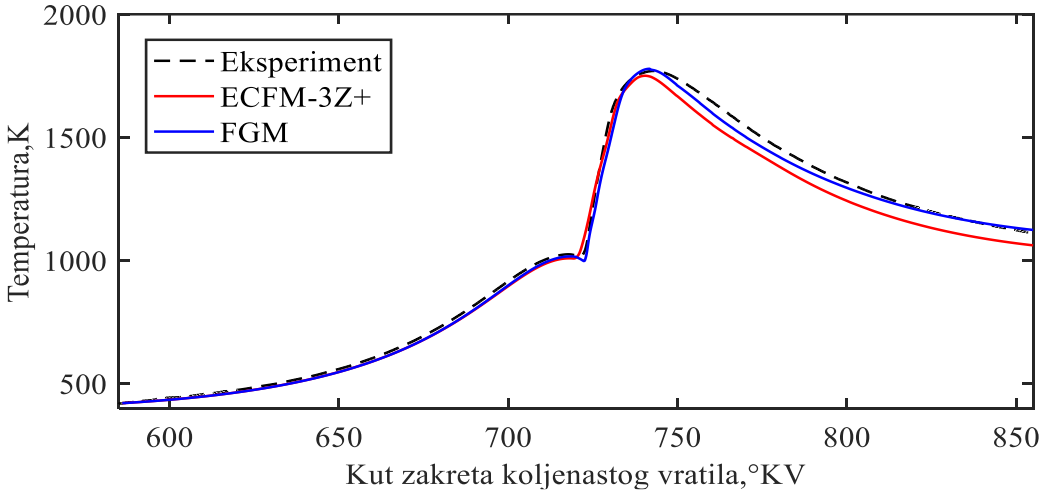

Slika 3. Usporedba po volumenu prosječne temperature za Slučaj 1

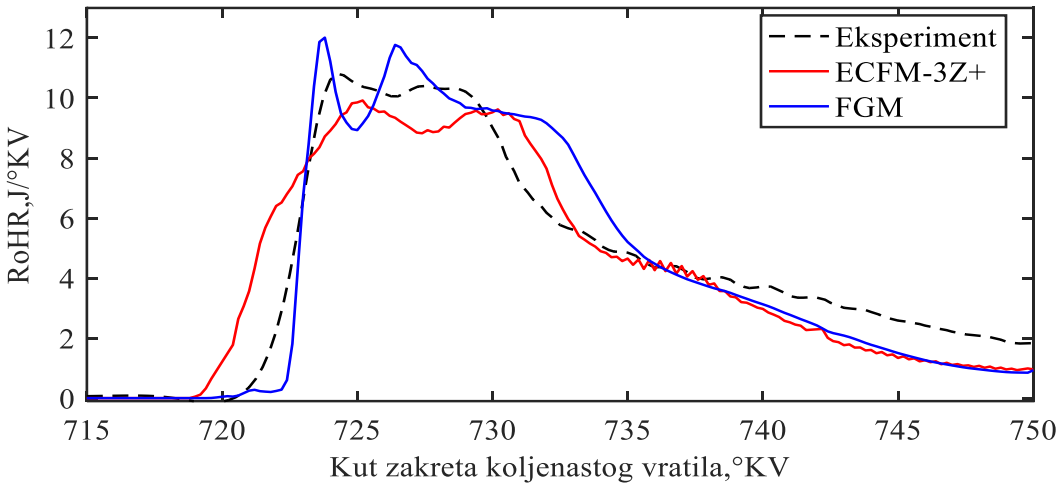

Slika 4. Usporedba brzine oslobađanja topline za Slučaj 1

Ista usporedba provedena je i za radne točke s tri ubrizgavanja. Slika 5 prikazuje usporedbu po volumenu prosječnog tlaka s eksperimentalnim podacima za Slučaj 3. Može se uočiti da je trend krivulja tlaka dobivenih modelima izgranja u Slučaju 3 sličan onima iz Slučaja 1. S krivuljom tlaka dobivenom FGM simulacijom ponovno se dobivaju nešto niže vrijednosti vršnog tlaka od eksperimentalnih podataka. Usporedba po volumenu prosječne temperature prikazana je Slika 6. Kao i kod radne točke s jednim ubrizgavanjem krivulja temperature dobivena FGM pristupom bolje prati eksperimentalnu krivulju u fazi ekspanzije u odnosu na rezultat ECFM-3Z+ simulacije. Oba modela izgranja dobro prate oblik eksperimentalne krivulje, međutim, daju nešto niže vrijednosti maksimalne temperature. Slika 7 prikazana je usporedba rezultata brzine oslobađanja topline. Iako ECFM-3Z+ simulacija dobro predviđa trenutak zapaljenja predubrizganog goriva, izgaranje istog odvija se prebrzo te se postiže veća maksimalna vrijednost u odnosu na eksperiment i rezultat FGM simulacije. Oba modela izgaranja izvrsno predviđaju početak zapaljenja goriva ubrizganog u glavnom ubrizgavanju i post-ubrizgavanju te su u tom dijelu krivulje dobivene s ECFM-3Z+ modelom i FGM pristupom sličnog oblika i dobro prate oblik eksperimentalne krivulje.

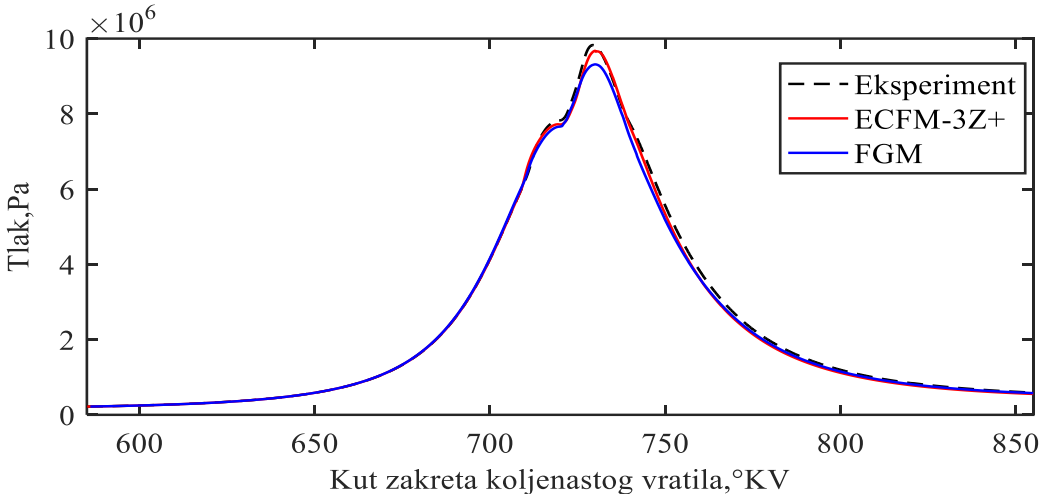

Slika 5. Usporedba po volumenu prosječnog tlaka za Slučaj 3

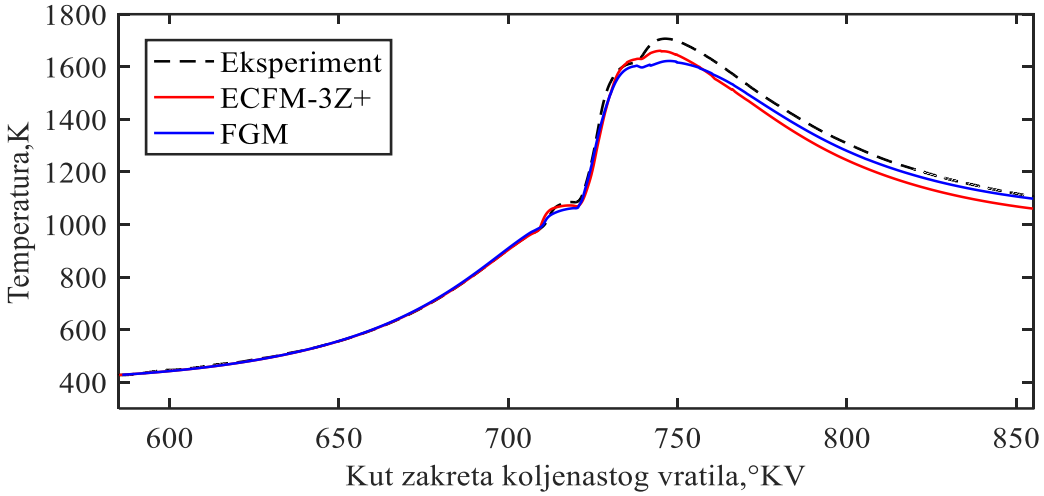

Slika 6. Usporedba po volumenu prosječne temperature za Slučaj 3

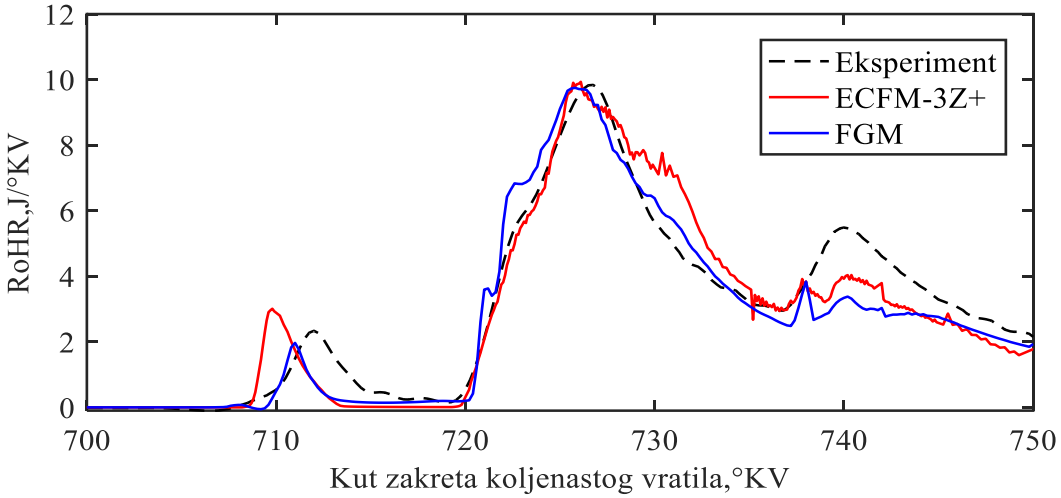

Slika 7. Usporedba brzine oslobađanja topline za Slučaj 3

Tablica 5 prikazana je usporedba NO emisija izračunatih numeričkim simulacijama s emisijama koje su mjerene tijekom eksperimenta u ispuhu motora. Rezultati su prikazani za iste radne točke za koje su prethodno analizirane krivulje tlaka, temperature i brzine oslobađanja topline. Uočava se da oba modela izgranja daju niže vrijednosti emisija NO-a od eksperimentalno izmjerenih, pri čemu FGM simulacija predviđa niže vrijednosti od ECFM-3Z+ simulacije. Trend eksperimentalnog smanjenja NO-a između Slučaja 1 i Slučaja 2 je dobro reproduciran s oba modela izgranja. Prikazani rezultati ukazuju na to da se oba modela izgaranja mogu koristiti za računanje emisija NO-a u dizel motorima.

Tablica 5. Maseni udio NO-a na kraju radnog ciklusa za Slučaj 1 i Slučaj 3

	Slučaj 1	Slučaj 3
Eksperiment (ppm)	135.6	119.1
ECFM-3Z+ (ppm)	133.02	83.7
FGM (ppm)	70.9	67.5

Tablica 6 prikazuje usporedbu vremena potrebnog za računanje procesa izgaranja korištenjem FGM pristupa s vremenom trajanja simulacije u kojoj se koristi ECFM-3Z+ model. Kao što se može vidjeti iz Tablica 6, FGM simulacije traju otpilike dva puta kraće od ECFM-3Z+ simulacija. Stoga, upotreba modela temeljenih na tabelaciji kemijskih vrsta u pred-procesiranju postaje sve popularnija.

Tablica 6. Usporedba trajanja simulacija

	Slučaj 1	Slučaj 3
ECFM-3Z+ (hh:mm)	1:52	2:54
FGM (hh:mm)	0:42	1:18

Budući da su oba korištena pristupa u modeliranju izgaranja validirana u odnosu na eksperimntalne podatke za radne točke s jednim ubrizgavanjem i s tri ubrizgavanja, može se zaključiti da su i ECFM-3Z+ model i FGM pristup sposobni za opisivanje procesa izgaranja u industrijskim dizel motorim

1. Introduction

Internal combustion (IC) diesel engine was invented roughly 200 years ago and is still under constant development in order to increase energy efficiency and satisfy strict environmental policies. Currently, compression ignition engines present a majority of truck engines, heavy-duty and marine engines, while in the European passenger cars, diesel fuel consumption is around three times larger than in the gasoline engines [1]. That can be addressed to higher specific power output, higher thermal efficiency, and better reliability of diesel engines [2]. As a result, diesel engines continue to provide diesel fuel as a substantial energy source in the transport sector, additionally justifying the need for further research and development in the field of combustion [3].

Extensive use of combustion systems features the main disadvantage that their harmful emissions have an adverse impact on the environment. The negative impact of combustion process on the environment can be mainly attributed to the greenhouse gases emissions such as carbon dioxide (CO_2), and the formation of pollutants such as nitrogen oxides (NO_x). Therefore, it is of the utmost importance to improve the combustion systems from this point forward, in order to avoid further pollution of the atmosphere. As a part of a tendency towards cleaner transport sector with lower impact on the environment, concentrations of the emitted pollutant emissions have been regulated in the past decade with the more stringent conditions that are enforced by the governmental policies every year. In order to meet the higher efficiency standards and emission regulations, the efficiency of diesel engines must be constantly improved. In recent times, combustion modelling employing computational fluid dynamics (CFD) in combination with experiment has become an irreplaceable tool in the engineering design process. The ability of numerical models to simulate complex physical and chemical processes together with experimental investigations has allowed engineers to reduce the costs and time of research and development. However, the numerical modelling of combustion systems is also challenging from a scientific point of view, since the interaction of the fluid flow, turbulence, chemical reactions and thermodynamics in reacting flows need to be solved simultaneously. Combustion process as a phenomenon of exceptional complexity can be numerically solved with detailed chemical kinetics or with the employment of approximated models. Detailed chemical kinetics provides a comprehensive insight into the chemical aspect of the combustion process with excessive computational demand. On the other hand,

combustion modelling approaches with a various degree of complexity have been introduced in the last two decades, in order to reduce the computational time. Therefore, a compromise must be found in order to satisfy a need for sufficiently accurate, but still computational affordable solutions. A good candidate in combustion modelling to satisfy that criteria is pre-tabulated chemistry approach. Pre-tabulated procedure where demanding chemistry calculations are decoupled from fluid flow solver allows applying detailed chemistry representation with an acceptable calculation time for the industrial applications. Within the utilised CFD code several combustion models are implemented, such as: eddy break up model, coherent flame model, probability density function (PDF) model, general gas-phase reaction model and steady combustion model. In the following section of the thesis, the description of combustion modelling by employing the coherent flame model and flamelet generated manifold reduction technique is shown.

1.1. Numerical modelling of the combustion process

Combustion modelling can be performed by using several different approaches such as computational demanding detailed chemical mechanisms, reduced mechanisms which are limited to a specific purpose and combustion models.

Chemical kinetics consists of the elementary reactions and chemical reaction rates, where the chemical reaction rate is the change in the number of reactants or product per unit time. An appropriate chemical mechanism has to be utilised to describe a fuel reaction process. Detailed chemical mechanisms contain a large number of chemical species and elementary reactions, which are experimentally validated and applied over an extensive set of conditions [4]. For example, the smallest mechanisms encountered in combustion modelling describe the oxidation of hydrogen where nine species and approximately fifty elementary reactions are involved [5]. For combustion of hydrocarbon fuels, as simple as methane (CH_4), the number of elementary reactions in the mechanism is much larger. Furthermore, for the combustion of higher hydrocarbons, such as diesel fuel, 2900 chemical species and 15009 elementary reactions have to be defined inside the chemical mechanism [6]. Such large mechanisms require significant computational resources for the simulation of industrial combustion systems, in order to calculate all interactions between elementary reactions that govern the combustion process. This computational demand increases with the number of chemical

species and reactions incorporated in the mechanism, and the number of mesh elements. Thus, different approaches have been addressed to reduce the computational expense of detailed reaction mechanisms.

One way to reduce the required number of equations that have to be solved is assuming that the chemical time and length scale in most flames are small. In the last decades, two main routes have been followed using this idea to model the detailed dynamics and structure of chemically reacting flows: chemical reduction techniques and laminar flamelet models.

Laminar flamelet methods are based on the idea that the flame structures are much thinner than most scales of the distortions in the flow, also implying that the chemical reactions are faster than all other time scales [7]. All flamelets models assume that the reaction takes place within relatively thin layers that separate the fresh unburned gas from the fully bunt gas. The internal structure of the flame is approximately frozen while it moves around in the flow. The dynamics of the thin flame front is predicted by computing a kinematic equation for the propagation of the flame front, mixture fraction equation for the mixing, and a CFD solver for the fluid flow [7]. One of the several laminar flamelet models, which has proven an ability to simulate the combustion process in internal combustion engines is extended coherent flame model (ECFM) developed by Colin et al. [8]. The ECFM belongs to the flame surface density type of approaches, which was first proposed in the context of diffusion flames in the work of Marble and Broadwell in 1997 [9]. More recently, this approach has been extended by considering a generalised flame surface density including all possible values of the mixture fraction, while reaction rates per unit of flame surface are provided by a library of transient diffusion flames [10]. Based on ECFM model, the unified diesel/petrol three-zones extended coherent flame model (ECFM-3Z) was briefly presented in [11]. In the ECFM-3Z, the description of unburned/burned gas is inherited from ECFM, as well as the premixed flame description based on the flame surface density equation. Each computational cell is split into three mixing zones: a pure fuel zone, a pure air plus possible residual gases (EGR) zone and a mixed zone, in order to account diffusion flame and mixing processes. This model is formulated and later validated by various researchers for partially-premixed and highly stratified combustion cases, as in case of gasoline direct injection (GDI) [12] and combustion cases with a high amount of exhaust gas recirculation (EGR) [13]. The work of [14] shows the capability of ECFM-3Z combustion model in predicting the combustion process and emission formation in a high-speed direct injection diesel engine. The ECFM-3Z applies to all types of combustion processes without the need for predefining the type of combustion that will be

encountered. Later, a new ECFM-3Z+ model was developed, that contains the basic equations of ECFM-3Z combustion model apart from the post-flame chemistry (equilibrium and CO oxidation reactions) which is extended in order to include better description of soot formation process [15].

Chemical reduction techniques are based on the idea that most of the chemical time scales in the system are very small. A time scale analysis can be performed if the fastest time scales are assumed to be in the steady-state and all transport processes are neglected. That means all variables can be stored in a database as a function of few controlling variables, and during the CFD solving procedure only the equations for the controlling variables are solved. Example of such reduction methods is the computational singular perturbation method from Lam and Goussis [16] and the intrinsic low-dimensional manifold approach of Maas and Pope [17].

In 1999, van Oijen and de Goey proposed a combination of the flamelet and the manifold approaches, referred to as the flamelet generated manifold (FGM) technique [18]. A recent review of the general FGM technique can be found in [19]. Successful application of the FGM combustion model, used in this work, for diesel engine was reported in [20]. Priesching et al. [21] showed a good prediction of the combustion process in a diesel engine case using FGM as well as the emission processes based on a large number of chemical reactions. The application of the FGM combustion model to gasoline engine simulations and knock analysis was reported by Goryntsev et al. [22]. Bekdemir et al. [23] demonstrated the utilisation of the FGM approach for simulating an ignition timing of diesel spray. The most critical characteristics like ignition delay and flame lift-off were well captured, demonstrating the potential of the FGM technique. Keum et al. [24] applied the FGM combustion model with the most detailed chemical reaction scheme as well as different surrogates to a canonical homogeneous charge compression ignition (HCCI) engine experiment from Sandia National Laboratory. Additionally, an application of various numerical approaches to access the knocking phenomena has been reported in publication [25].

In this thesis, the AVL FIRE™ CFD software is used to predict the combustion in a diesel engine by employing the previously described combustion models, the FGM and the ECFM3Z+. Combustion and emission results are compared to available experimental data from the real industrial IC engine. The calculated results were validated for both single and multi-injection strategy. This work is structured as follows. First, in Chapter 2, the mathematical model used for performing a numerical investigation is described. Secondly, numerical setup,

regarding the generated computational mesh and solver settings, is presented in Chapter 3. The results are presented and discussed in Chapter 4. Finally, in Chapter 5 the conclusions are derived.

2. Mathematical model

The following chapter will describe, in some detail, mathematical models relevant to the thesis. Initially, the main transport equations for CFD are presented. Afterwards, a short introduction into turbulent flows is provided followed by the explanation of the $k-\zeta-f$ turbulence model. Furthermore, the concept of multiphase flows is introduced, emphasizing the Euler Lagrangian approach for spray modelling along with its submodels. Additionally, chemistry modelling is explained, providing information on the FGM and ECFM approaches. Finally, the models used for NO_x emission formation are introduced.

2.1. General transport equation

The general transport equation represents one of the constitutional equations of continuum mechanics. It is the core equation describing how a scalar quantity is transported in a defined space. Many equations describing fluid flow are just versions of the general transport equation:

$$\frac{\partial}{\partial t}(\rho\varphi) + \frac{\partial}{\partial x_j}(\rho\varphi u_j) = \frac{\partial}{\partial x_j}\left(\Gamma_\varphi \frac{\partial \varphi}{\partial x_j}\right) + S_\varphi \tag{2.1}$$

In the general transport equation, φ is a generic transported variable, Γ is the diffusion coefficient and S_φ is a volume source or sink of the transported variable φ.

The first term on the left-hand side of Eq. (2.1) is the unsteady term which represents the inertia of the system. The second term is the convection term which represents the convective transport by prescribed velocity field, the term is of hyperbolic nature. The right-hand side of Eq. (2.1) contains diffusion and source/sink terms. Diffusion term represents gradient transport and is of elliptic nature. Sources and sinks account for non-transported effects: local volume production and destruction of the transported variable φ. By substituting the transported variable φ in the general transport equation with appropriate property (mass, momentum, energy, etc.), the fundamental governing equations of fluid flow can be derived.

2.1.1. Mass conservation

The mass conservation equation or continuity equation can be derived from the general transport equation by setting φ to 1. As there is no diffusion of mass, no diffusion term exists

in the equation. Likewise, there is also no source or sink term, as mass is assumed to be impossible to vanish or be generated. Hence, the expression for the mass conservation in the conservative (flux) form is defined as:

$$\frac{\partial \rho}{\partial t} + \frac{\partial}{\partial x_j}(\rho u_j) = 0 \tag{2.2}$$

2.1.2. Momentum conservation

The momentum conservation law is derived according to Newton's second law and it states that the sum of the volume and surface forces acting on a fluid control volume element is equal to the time rate of momentum change of the fluid control volume element. Differential form of the momentum conservation law is given with Eq. (2.3):

$$\frac{\partial}{\partial t}(\rho u_i) + \frac{\partial}{\partial x_j}(\rho u_j u_i) = \rho f_i + \frac{\partial \sigma_{ji}}{\partial x_j} \tag{2.3}$$

The conservation of momentum represents a vector equation that comprises three momentum equations (i = 1,2,3). Each equation describes the values of momentum change in the Cartesian coordinate system. The left-hand side of the equation represents the temporal and spatial change of the momentum. The right-hand side of Eq. (2.3) is the sum of volume and surface forces acting on the fluid within the control volume. The first term denotes the volume forces such as gravitational and centrifugal forces. The second term indicates the surface forces which can be produced as an effect of the existence of a pressure gradient and by the viscous stresses in the fluid, defined as:

$$\sigma_{ji} = -p\delta_{ji} + \tau_{ji} \tag{2.4}$$

In Eq. (2.3) the term p is absolute pressure, δ_{ji} is the Kronecker delta and τ_{ji} is viscous stress. For Newtonian fluids, the viscous stress tensor can be expressed as:

$$\tau_{ji} = 2\mu D_{ji} - \frac{2}{3}\mu \frac{\partial u_k}{\partial x_k}\delta_{ji} \tag{2.5}$$

Where μ is molecular viscosity coefficient and D_{ji} is the rate of deformation tensor:

$$D_{ji} = \frac{1}{2}\left(\frac{\partial u_j}{\partial x_i} + \frac{\partial u_i}{\partial x_j}\right) \tag{2.6}$$

Combining the Eq. (2.3)-(2.6) and defining the body force as the gravitational force (ρg_i) the most general form of Navier-Stokes equations for Newtonian fluids can be obtained:

$$\frac{\partial}{\partial t}(\rho u_i) + \frac{\partial}{\partial x_j}(\rho u_j u_i) = \frac{\partial}{\partial x_j}\left(\left(\frac{\partial u_j}{\partial x_i} + \frac{\partial u_i}{\partial x_j}\right) - \frac{2}{3}\mu\frac{\partial u_k}{\partial x_k}\right) + \rho g_i - \frac{\partial p}{\partial x_i} \quad (2.7)$$

2.1.3. Energy conservation

The energy equation is derived by following the physical principle that the amount of energy cannot be created or destroyed, it can only be converted from one form to another but the total energy within the domain remains constant. The conservation of energy is derived from the First law of thermodynamics. The equation can be written in terms of specific total energy e, deriving from the general transport equation:

$$\frac{\partial}{\partial t}(\rho e) + \frac{\partial}{\partial x_j}(\rho u_j e) = \rho g_i u_i + \frac{\partial}{\partial x_j}(\sigma_{ji} u_i) - \frac{\partial q_i}{\partial x_i} + S_v \quad (2.8)$$

The first term on the left-hand side is the one which describes the temporal variation of energy in the fluid. The second term is the convective term and it determines the convective flux of energy in the fluid. The first term on the right-hand side is the gravitational force term. The second term describes the rate of work due to the existence of surface forces. The third term on the right-hand side is the diffusive term and it describes the heat flux due to the existence of a temperature gradient. The last term denotes the distributed internal heat source/sink due to radiation, chemical reactions or any other volumetric heat source.

The heat flux represents heat transfer by diffusion, and it is governed by Fourier's law:

$$q_i = -\lambda\frac{\partial T}{\partial x_i}\ , \quad (2.9)$$

where λ denotes the thermal conductivity coefficient.

2.1.4. Species conservation

When the chemical reactions are involved, as they are in combustion modelling, the transport equations for the different chemical species in the domain need to be solved. The species mass conservation equation, unlike the continuity equation, contains the source term as species can form or be destroyed through chemical reactions:

$$\frac{\partial}{\partial t}(\rho Y_i) + \frac{\partial}{\partial x_j}(\rho u_j Y_i) = \frac{\partial}{\partial x_j}\left(\Gamma\frac{\partial Y_i}{\partial x_j}\right) + S_{Y_i} \quad (2.10)$$

where Y_i is the mass fraction of the i - th chemical species defined as:

$$Y_i = \frac{m_i}{m} \tag{2.11}$$

In Eq. (2.11) term m_i is the mass of species i, and m is total mass. The first term on the left side of Eq. (2.10) is the time derivative, while the second term is the species convective transport. The first term on the right-hand side is the diffusion term which is modelled by Fick's law of diffusion. The last term on the right side is the source/sink term due to chemical reactions.

2.2. Turbulence modelling

Turbulent flows occur in most engineering applications, and there are many methods developed for prediction of such flows which differ in the level of detail the flow is resolved [26]. Direct numerical simulation (DNS) is the most detailed approach to turbulence modelling, and it numerically solves the governing equations over the whole range of turbulent scales. This approach requires high spatial and temporal resolution, demanding substantial computational resources and long simulation times, making DNS unsuitable for the most engineering applications. Large eddy simulation (LES) is an approach where the large-scale eddies are resolved, and the small eddies are modelled. Therefore, this approach requires a spatial filter separating the large scales from the small ones. LES is also too demanding to become conventional in the industry.

The most favoured method for modelling turbulent flows in industrial applications is Reynolds averaged Navier-Stokes equations (RANS) with an appropriate turbulence model. The basic idea of this model is to describe the variables of interest into fluctuating and mean values reducing the computational demand. The RANS equations have a similar form to those of the original Navier-Stokes (conservation) equations derived in the previous section. Two additional terms, the Reynolds stresses and the turbulent heat flux appear due to the averaging of the process. They must be modelled by the turbulence model in order to close the system of equations. In this thesis, the $k - \zeta - f$ turbulence model is employed, which is explained in the following section.

2.2.1. The $k-\zeta-f$ turbulence model

The $k-\zeta-f$ turbulence model is based on Durbin's concept of elliptical relaxation [27], and it solves an additional transport equation for the velocity scale ratio $\zeta = \overline{v^2}/k$. It is robust and suitable for spray process modelling, and for describing the swirl motion which is characteristic for IC diesel engines [28]. The eddy-viscosity is obtained from:

$$v_t = C_\mu \zeta \frac{k^2}{\varepsilon}, \tag{2.12}$$

where C_μ is the model constant, k is the turbulent kinetic energy, ε is the turbulent kinetic energy dissipation rate, and ζ is the velocity scale ratio. Other variables are determined according to:

$$\rho \frac{Dk}{Dt} = \rho(P_k - \varepsilon) + \frac{\partial}{\partial x_j}\left[\left(\mu + \frac{\mu_t}{\sigma_k}\right)\frac{\partial k}{\partial x_j}\right], \tag{2.13}$$

$$\rho \frac{D\varepsilon}{Dt} = \rho \frac{C_{\epsilon 1}^* P_k - C_{\epsilon 2}\varepsilon}{T} + \frac{\partial}{\partial x_j}\left[\left(\mu + \frac{\mu_t}{\sigma_k}\right)\frac{\partial \varepsilon}{\partial x_j}\right], \tag{2.14}$$

$$\rho \frac{D\zeta}{Dt} = \rho f - \rho \frac{\zeta}{k} P_k + \frac{\partial}{\partial x_j}\left[\left(\mu + \frac{\mu_t}{\sigma_k}\right)\frac{\partial \zeta}{\partial x_j}\right]. \tag{2.15}$$

Elliptic function f is calculated as:

$$f - \frac{\partial^2 f}{\partial x_i \partial x_j} L^2 = \left(C_1 + C_2 \frac{P_k}{\zeta}\right)\frac{2/3 - \zeta}{T}, \tag{2.16}$$

where the turbulent length L and turbulent time t_t, are derived from Eq. (2.17):

$$\begin{aligned} L &= C_L \max\left[min\left(\frac{k^{1.5}}{\epsilon}, \frac{k^{0.5}}{\sqrt{6}C_\mu |S| \zeta}\right), C_\eta \left(\frac{v^3}{\epsilon}\right)^{0.25}\right], \\ t_t &= \max\left[min\left(\frac{k}{\epsilon}, \frac{0.6}{\sqrt{6}C_\mu |S| \zeta}\right), C_T \left(\frac{v}{\epsilon}\right)^{0.5}\right]. \end{aligned} \tag{2.17}$$

2.3. Spray modelling

The spray process is used to distribute the liquid in a broader area, and to increase the surface needed for the more intensive evaporation process. In IC engines, the spray is produced by a high-pressure liquid fuel injection through a small diameter nozzle. It is a common knowledge that the combustion efficiency, combustion stability and pollutant formation depend on the spray process [26]. Therefore, an understanding of such a process is necessary for further development of various engineering applications.

The spray is a two-phase fluid flow of gas and liquid droplets in which the liquid phase is strongly dispersed in the gaseous one. In general, there are two approaches for multiphase flow modelling: Euler-Euler approach (CDM – continuous droplet model) and Euler-Lagrangian approach (DDM – dispersed droplet model). In this thesis, as in the current engineering applications, the conventional Euler-Lagrangian method for solving the multiphase flow is used. In the Euler-Lagrangian approach, the spray droplets are represented by finite number of droplet groups called parcels. It is assumed that all droplets within one parcel are similar in size and have the same physical properties. The motion and the transport properties of the parcels are tracked through the flow field using a Lagrangian formulation, while the gas phase is described by solving conservation equations using the Eulerian formulation. The coupling between the liquid and the gaseous phase is considered by introducing appropriate source terms for interfacial mass, momentum and energy exchange. The force that has the highest impact on spray formation is the drag force that is generated due to relative velocities. In the transport equations, the trajectory and velocity of a parcel are derived from Newton's second law of motion:

$$m_p \frac{du_{id}}{dt} = \sum F_i \tag{2.18}$$

Where m_p is the parcel mass and $\sum F_i$ is the sum of all forces acting upon the parcel. The trajectory of parcel x_{pi} is calculated by integrating parcel velocity:

$$x_{pi}(t) = \int_t^{t+\Delta t} u_{pi} dt \tag{2.19}$$

To adequately capture the spray phenomena, several sub-models are introduced, such as the primary and secondary breakup, evaporation, droplet deformation, collision and turbulent dispersion. These sub-models enable appropriate handling of physical process that would otherwise not be covered by the general transport equations [29]. The main disadvantage of

this approach is that the computational effort rises with the increasing parcel number. Therefore, such a method is usually used to model the sufficiently diluted spray where the volume fraction of the dispersed phase is lower [30].

2.3.1. Wave breakup model

The most suitable breakup model for high-pressure direct injection is the standard Wave model [31]. The Wave breakup model is based on the Kelvin-Helmholtz instability of liquid jet, where the viscous forces produce waves on the liquid surface, and new droplets are formed from the surface waves. Waves grow on the droplet surface with rate Ω and a wavelength A. The size of the newly formed droplets is determined from the wavelength and growth rate of this instability. The breakup of the initial droplets results in the production of new droplets and the reduction of the size of the parent droplets [32].

The rate of radius reduction of the parent drops is expressed as:

$$\frac{dr}{dt} = -\frac{(r - r_{stable})}{\tau_a}, \tag{2.20}$$

with r_{stable} representing the product droplet radius and τ_a is the breakup time of the model, which can be calculated as:

$$\tau_a = \frac{(3.726 \cdot C_2 \cdot r)}{A \cdot \Omega}. \tag{2.21}$$

The product droplet radius is expressed proportionally to the wavelength A of the fastest growing wave on the parcel surface:

$$r_{stable} = A \cdot C_1\,, \tag{2.22}$$

where C_1 is the Wave model constant, which is set to the recommended value of 0.61 [33]. The second model constant C_2 corrects the characteristic breakup time and varies from one injector to another. Higher values of C_2 slows down the disintegration process. The wave length A and wave growth rate Ω depend on the local flow properties.

$$\begin{aligned} A &= 9.02 \cdot r \frac{(1 + 0.45 \cdot Oh^{0.5})(1 + 0.4 \cdot T^{0.7})}{\left(1 + 0.87 \cdot We_g^{1.67}\right)^{0.6}}, \\ \Omega &= \left(\frac{\rho_d r^3}{\sigma}\right)^{-0.5} \frac{0.34 + 0.38 \cdot We_g^{1.5}}{(1 + Oh)(1 + 1.4T^{0.6})}. \end{aligned} \tag{2.23}$$

In the equations above, σ is the surface tension and We, and Oh are Weber and Ohnesorge number defined as:

$$We = \frac{2r\rho u^2}{\sigma},$$
$$Oh = \frac{\mu}{\sqrt{2r\rho\sigma}} = \frac{\sqrt{We}}{Re}, \tag{2.24}$$

as well as $T = OhWe^{0.5}$.

2.3.2. Abramzon evaporation model

Besides the liquid ligaments and droplets breakup, simultaneously in the spray region, the evaporation process is ongoing. It influences global spray parameters and secondary breakup as well. It results from the fact that the evaporation process leads to decrease of the droplet diameters while they move along the gaseous environment. The mathematical model used in this thesis to perform the calculation of the evaporation process is Abramzon and Sirignano approach. This approach relies on the classic film theory where the resistances to heat and mass transfer are modelled by fictional gas films of constant thickness: δ_T and δ_m [34]. In the case of evaporating droplet, these film thickness values need to be corrected by the factors F_T and F_M. Droplet evaporation is described by the empirical Nusselt and Sherwood laws derived from experiments using single droplet under certain conditions. Consequently, the droplet evaporation rate is given as [33]:

$$\dot{m} = \pi\overline{\rho_g} D_d Sh \cdot \ln(1 + B_M),$$
$$\dot{m} = \pi \frac{\overline{k_g}}{\overline{c_{pF}}} D_d Nu \cdot \ln(1 + B_T), \tag{2.25}$$

where D_d is the droplet diameter, and $\overline{\rho_g}$, $\overline{\beta_g}$, $\overline{k_g}$ are respectively average density, binary diffusion coefficient and thermal conductivity of the gas mixture at reference conditions, $\overline{c_{pF}}$ is the average specific heat capacity of the vapour. The Nusselt and Sherwood numbers are the non-dimensional parameters which are calculated by the numbers Sh_0 and Nu_0 of the non-evaporating droplet and the corresponding correction factors for the film thickness F_M and F_T:

$$Sh^* = 2 + \frac{Sh_0 - 2}{F_M}; \quad Sh_0 = 2 + 0.552Re^{1/2}Sc^{1/3}, \tag{2.26}$$

$$Nu^* = 2 + \frac{Nu_0 - 2}{F_T}; \quad Nu_0 = 2 + 0.552Re^{1/2}Pr^{1/3}. \tag{2.27}$$

The values B_M and B_T are the mass and heat transfer numbers, also called Spalding numbers, that can be calculated by the following terms:

$$B_M = \frac{Y_{FS} - Y_\infty}{1 - Y_{FS}}, \tag{2.28}$$

$$B_T = \frac{\overline{c_{pF}}(T_\infty - T_s)}{L(T_s) + \frac{Q_L}{\dot{m}}}. \tag{2.29}$$

In equations above Y_{FS} is the fuel mass fraction, and $L(T_s)$ is the latent heat of vaporisation at a temperature T_s. Index S denotes the condition at a droplet surface, while index ∞ denotes the ambient condition.

2.4. Combustion modelling

The fuel combustion is a process of heat release due to the chemical reactions of the fuel vapour species and an oxidizer [5]. The combustion modelling is a complicated phenomenon that accounts hundreds of different compounds of chemical scalars and reactions in the calculation domain. The process can be described through combustion models with different level of complexity or by employing detailed chemical mechanisms. In the following section, the description of two different combustion models, used in this thesis, is introduced.

2.4.1. ECFM-3Z+ model

The three-zones extended coherent flame model (ECFM-3Z+) is derived from the classical flame surface density-based combustion model, namely, coherent flame model (CFM) [9]. A particularly attractive feature of CFM is the effective separation of the details of the chemistry from the details of the turbulent structure. The model is fully coupled with the spray model and enables to model stratified combustion with EGR effects and pollutant formation. In this model, it is assumed that the chemical time scales are much smaller than turbulent ones. CFM approximates the turbulent flame as a series of a small laminar flame element called a flamelet. The model also assumes that the reactions occur within relatively thin layers that separate the fresh unburned gas from the wholly burnt gas. In this model, the rate at which reactants are consumed is the product of flame surface density and reacting rate per unit flame surface [15]:

$$\overline{\rho \dot{r}_{fu}} = -\omega_L \sum , \tag{2.30}$$

with ω_L as the mean laminar fuel consumption rate per unit surface along the flame front and $\sum$ as the flame surface density.

Each cell of computational mesh is split into three mixing zones to account diffusion and mixing processes, as shown in Figure 1: a pure fuel zone, a pure air plus possible residual gases (EGR) zone and a mixed zone. The three zones are too small to be resolved by the mesh, and thus the zones are modelled as sub-grid quantities. The mixed zone is the result of turbulent and molecular mixing between gases in the other two zones and is located at the flame front.

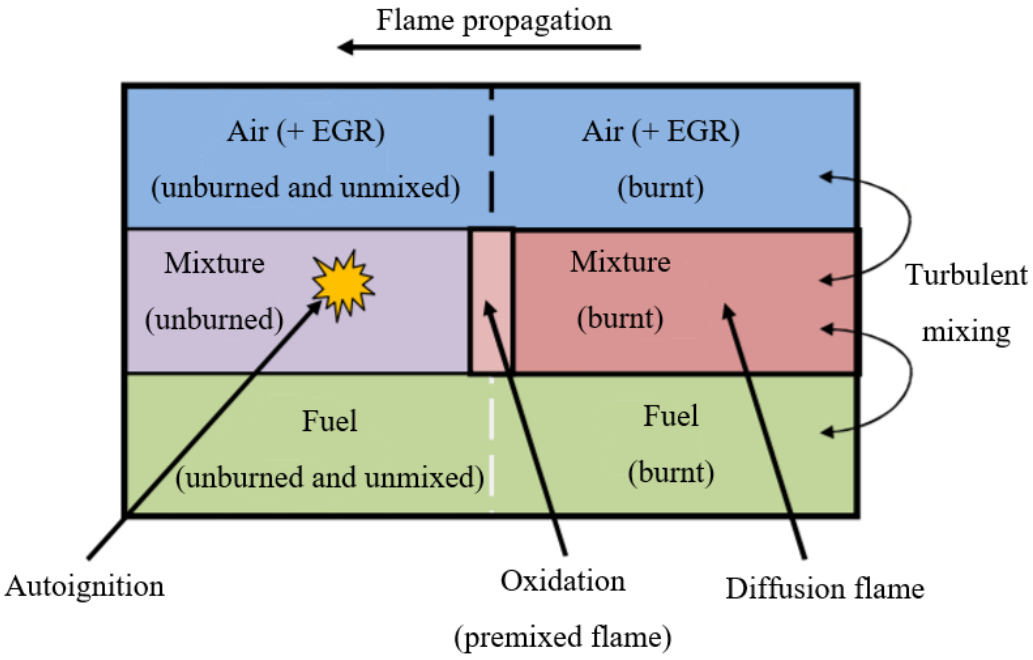

Figure 1. Zones in ECFM-3Z+ model [9]

Besides the standard species transport equations, the ECFM-3Z+ solves additionally transport equations of 11 chemical species: $O_2, N_2, CO_2, CO, H_2, H_2O, O, H, N, OH$ and NO in each cell [2]:

$$\frac{\partial \bar{\rho} y_x}{\partial t} + \frac{\partial \bar{\rho} u_i y_x}{\partial x_i} - \frac{\partial}{\partial x_i}\left(\left(\frac{\mu}{S_c} + \frac{\mu_t}{S_{ct}}\right)\frac{\partial y_x}{\partial x_i}\right) = \overline{\dot{\omega}_x} \tag{2.31}$$

Where $\overline{\dot{\omega}_x}$ is the combustion source term and y_x is averaged mass fraction of species *x*. Furthermore, three transport equations for the fuel mass fraction y_{fu}, mixture fraction *f* and residual gas mass *g* have to be solved [2]:

$$\frac{\partial}{\partial t}(\rho y_{fu}) + \frac{\partial}{\partial x_i}(\rho u_i y_{fu}) = \frac{\partial}{\partial x_i}\left(\Gamma_{fu}\frac{\partial y_{fu}}{\partial x_i}\right) + S_{fu}, \tag{2.32}$$

$$\frac{\partial}{\partial t}(\rho f) + \frac{\partial}{\partial x_i}(\rho u_i f) = \frac{\partial}{\partial x_i}\left(\Gamma_f\frac{\partial f}{\partial x_i}\right), \tag{2.33}$$

$$\frac{\partial}{\partial t}(\rho g) + \frac{\partial}{\partial x_i}(\rho u_i g) = \frac{\partial}{\partial x_i}\left(\Gamma_g\frac{\partial g}{\partial x_i}\right). \tag{2.34}$$

The fuel fraction is divided into two variables: fuel mass fraction in the fresh gases $y_{u.f.}$ and fuel mass fraction in burnt gases. Where the fuel mass fraction in the fresh gases $y_{u.f.}$ is calculated from the transport equation:

$$\frac{\partial \bar{\rho} y_{u.f.}}{\partial t} + \frac{\partial \bar{\rho} u_i y_{u.f.}}{\partial x_i} = \frac{\partial}{\partial x_i}\left(\left(\frac{\mu}{Sc} + \frac{\mu_t}{Sc_t}\right)\frac{\partial y_{u.f.}}{\partial x_i}\right), \tag{2.35}$$

and the fuel mass fraction in burnt gases is calculated as the difference between the fuel mass fraction y_{fu} and fuel mass fraction in the fresh gases $y_{u.f.}$. Two new quantities are introduced to describe the mixing zones: the unmixed fuel y_{Fu}^F and the unmixed oxygen y_{O2}^A. The equations for these unmixed species are [33]:

$$\frac{\partial \bar{\rho} y_{Fu}^F}{\partial t} + \frac{\partial \bar{\rho} u_i y_{Fu}^F}{\partial x_i} - \frac{\partial}{\partial x_i}\left(\frac{\mu}{Sc}\frac{\partial y_{Fu}^F}{\partial x_i}\right) = \bar{\rho}\dot{S}_f - \frac{1}{\tau_m} y_{Fu}^F\left(1 - y_{Fu}^F\frac{\bar{\rho} M_{mix}}{\overline{\rho_u} M_f}\right), \tag{2.36}$$

$$\frac{\partial \bar{\rho} y_{O2}^A}{\partial t} + \frac{\partial \bar{\rho} u_i y_{O2}^A}{\partial x_i} - \frac{\partial}{\partial x_i}\left(\frac{\mu}{Sc}\frac{\partial y_{O2}^A}{\partial x_i}\right) = -\frac{1}{\tau_m} y_{O2}^A\left(1 - \frac{y_{O2}^A}{y_{O2}^\infty}\frac{\bar{\rho} M_{mix}}{\overline{\rho_u} M_{air+EGR}}\right), \tag{2.37}$$

where the source terms depend on the mixing time which considers turbulence quantities and is defined as:

$$\frac{1}{\tau_m} = \beta\frac{\varepsilon}{k}, \tag{2.38}$$

where the is a model factor with the value 1.

2.4.2. Flamelet generated manifold

The flamelet generated manifold (FGM) method is based on the combination of two approaches, the flamelet approach and the manifold approach, which reduce the equations to be solved and thus cutting down the computational time [20]. The model shares the idea that a turbulent flame is an ensemble of thin, laminar, locally one-dimensional flames, called flamelets, embedded within the turbulent flow field. The flamelet assumption states that most

variables, like species concentrations and temperature, can be assumed to be dependent on a small number of control variables relevant for the flamelets. The implementation of FGM method is typical for manifold method, which means that combustion chemistry is pre-computed and relevant data is stored in a multi-dimensional database (look-up table) and interpolated during the CFD simulations as illustrated in Figure 2.

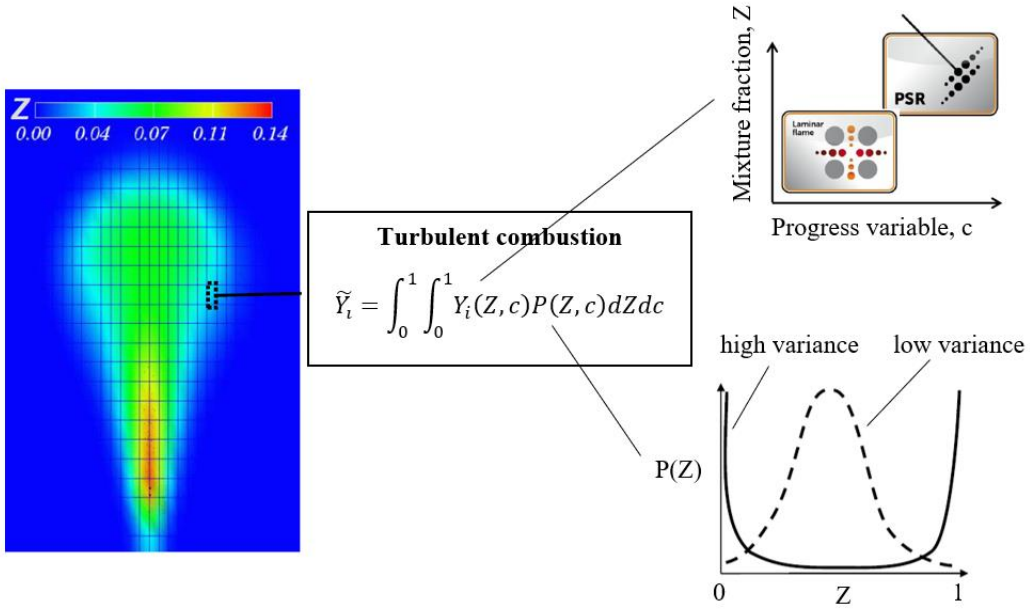

Figure 2. Flow chart of FGM combustion model [35]

Detailed chemistry is used to create the look-up tables, which are based on ignition homogeneous reactor chemistry calculations and have up to 8 dimensions: pressure, temperature, progress variable and its variance, mixture fraction and its variance, exhaust variable (EGR) and fuel composition parameter. PDF approach is used to account the turbulence effects on the flame structure. Figure 3 visualises the output of 0D perfectly stirred reactor (PSR) simulations for two different temperatures: a) T=1200 K, b) T=1700 K, where CO mass fraction data is mapped on a predefined progress variable and mixture fraction grid. It is visible that the CO mass fraction increases as the combustion process propagates from the fresh to burnt gas. Furthermore, the peek values for different progress variable values are achieved at mixture fraction value which approximately corresponds to the value of stoichiometric mixture. The increase in temperature also leads to an increase in CO mass fraction.

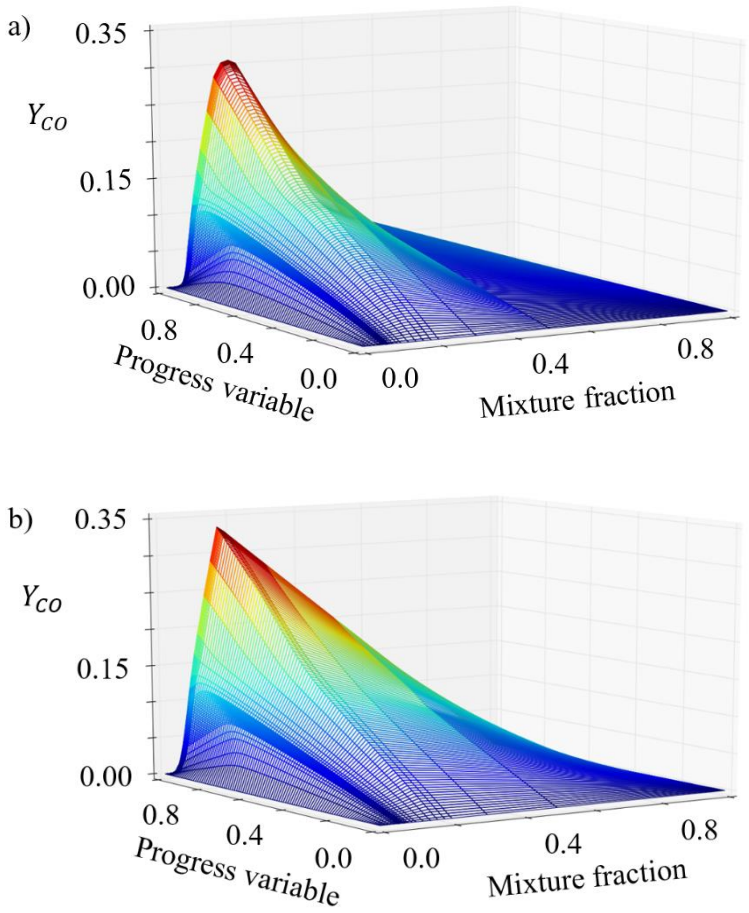

Figure 3. FGM table visualisation: a) T=1200 K , b) T=1700 K

In addition to the transport equations of the turbulence model, four scalar transport equations for progress variable *c*, progress variable variance c_{var}, mean mixture fraction Z, and mixture fraction variance Z_{var} need to be solved.

Mixture fraction is a conserved scalar used to describe the mixing process between fuel and air. When using liquid fuels, the mixture fraction equation has a spray source term. The mean mixture fraction and its variance equations can be described as follows [15]:

$$\frac{\partial}{\partial t}\left(\bar{\rho}\tilde{Z}\right)+\frac{\partial}{\partial x_i}\left(\bar{\rho}\tilde{u}_i\tilde{Z}\right)=\frac{\partial}{\partial x_i}\left(\bar{\rho}(D+D_T)\frac{\partial\tilde{Z}}{\partial x_i}\right)+\overline{\dot{S}_{vap}}, \tag{2.39}$$

$$\frac{\partial}{\partial t}\left(\bar{\rho}\widetilde{Z''^2}\right)+\frac{\partial}{\partial x_i}\left(\bar{\rho}\tilde{u}_i\widetilde{Z''^2}\right)=\frac{\partial}{\partial x_i}\left(\bar{\rho}(D+D_T)\frac{\partial\widetilde{Z''^2}}{\partial x_i}\right)+2\bar{\rho}D_T\left(\frac{\partial\widetilde{Z''}}{\partial x_i}\right)^2+\bar{\rho}\widetilde{\chi_Z}, \tag{2.40}$$

where the scalar dissipation rate is:

$$\widetilde{\chi_Z}=2\frac{\varepsilon}{k}\widetilde{Z''^2}\,. \tag{2.41}$$

Progress variable is a scalar describing the reaction progress from fresh to burnt gas. When normalised, it is zero in fresh gas and unity in the burnt gas, and it has a source term from chemistry. The progress variable is often defined as a linear combination of certain species, for example:

$$Y_C = \frac{Y_{CO}}{W_{CO}} + \frac{Y_{CO2}}{W_{CO2}}, \tag{2.42}$$

where dominant species CO and CO_2 are used, weighted by their respective molecular weights. The progress variable can be normalised as follows:

$$c = \frac{Y_C}{Y_C^{EQ}}. \tag{2.43}$$

The transport equations for the normalised mean progress variable and its variance is written as:

$$\frac{\partial}{\partial t}(\bar{\rho}\tilde{c}) + \frac{\partial}{\partial x_i}(\bar{\rho}\tilde{u_\iota}\tilde{c}) = \frac{\partial}{\partial x_i}\left(\bar{\rho}(D + D_T)\frac{\partial \tilde{c}}{\partial x_i}\right) + \bar{\dot{S}_c}, \tag{2.44}$$

$$\frac{\partial}{\partial t}\left(\bar{\rho}\widetilde{c''^2}\right) + \frac{\partial}{\partial x_i}\left(\bar{\rho}\tilde{u_\iota}\widetilde{c''^2}\right) = \frac{\partial}{\partial x_i}\left(\bar{\rho}(D + D_T)\frac{\partial \widetilde{c''^2}}{\partial x_i}\right) + 2\bar{\rho}D_T\left(\frac{\widetilde{\partial c''}}{\partial x_i}\right)^2 + \bar{\rho}\widetilde{\mathcal{X}_c}, \tag{2.45}$$

where the scalar dissipation rate is:

$$\widetilde{\mathcal{X}_c} = 2\frac{\varepsilon}{k}\widetilde{c''^2}. \tag{2.46}$$

The look-up tables enable reduction of the number of species to five, with the retention of correct thermochemistry. The used chemical species are O_2, CO_2, H_2O, N_2 and virtual fuel. Virtual fuel is an artificial species with the same physical and thermochemical properties as the actual fuel, and it burns in one single step. The virtual fuel [36] allows imposing species mass fractions from the look-up table, thus comprising all combustible matter present in the real burning mixture. The rate of change of the virtual fuel mass fraction is computed using:

$$\dot{Y_{VF}} = \frac{Y_{VF}(c(t + \Delta t), coords) - Y_{VF}(c(t), coords)}{\Delta t} \tag{2.47}$$

The rate of change of the other species of the virtual system is calculated by the CFD code, based on stoichiometric coefficients.

The chemical heat source term is computed from species change rates $\dot{\omega}_\iota$ and their partial enthalpies h_s :

$$\dot{\omega_{heat}} = \dot{\rho} \sum_{i} \dot{\omega_i} h_i \,. \tag{2.48}$$

2.5. Emission modelling

In ideal conditions, when the complete diesel fuel combustion is achieved, solely the CO_2 and H_2O species would be generated. However, such conditions are impossible to achieve due to the engine transient operating conditions. In addition, several other harmful species, such as CO, hydrocarbons, particulate matter (PM) and NO_x are produced [37]. A significant part of these pollutant emissions is NO_x pollutants, while the second biggest emission share belongs to the PM emissions. More than 50% of the total PM emissions from diesel engines are soot [38]. Nitrogen oxides (NO_x) consists of nitric oxide (NO), nitrogen dioxide (NO_2) and nitrous oxide (N_2O). They are collectively referred to as NO_x. The NO is the main component of NO_x in diesel engines. According to [39] NO_2 and especially N_2O emissions are not significant within diesel engines. Nitric oxide (NO) is formed in combustion chamber by three mechanisms [15]:

- Thermal NO mechanism forms nitrogen oxide in post-flame regions by oxidation of nitrogen. Due to the high activation energy required to decompose the strong N_2 triple bond thermal NO is formed at high temperatures (T > 1800 K) [15];
- Prompt NO is formed in reaction of molecular nitrogen with hydrocarbon radicals. It is characterized by its fast formation (hence prompt);
- Fuel NO is formed due to the presence of the nitrogen in the fuel.

Fuel NO formation can principally be neglected during the combustion process in IC engines since there is no significant amount of nitrogen in the fuel. Therefore, in this thesis only thermal and prompt mechanisms are considered in the calculation procedure.

2.5.1. Extended Zeldovich model

Zeldovich suggested that the thermal NO mechanism can be decoupled from the primary combustion process if the equilibrium of temperature and species is assumed. Therefore, the extended Zeldovich mechanism is a powerful post-processing tool that can be applied to any data set without requiring the recalculation of the primary combustion process.

The reaction mechanism considers the effects of oxygen, nitrogen and hydrogen radical on thermal NO formation and the process is described by the following set of chemical reactions:

$$N_2 + O \overset{k1}{\leftrightarrow} NO + N \tag{2.49}$$

$$N + O_2 \overset{k2}{\leftrightarrow} NO + O \tag{2.50}$$

$$N + OH \overset{k3}{\leftrightarrow} NO + H \tag{2.51}$$

It is essential to point out that all three chemical reactions that represent the Zeldovich mechanism exhibit strong temperature dependency. Derived from the above equations, the overall NO formation rate can be described as follows:

$$\frac{dc_{NO}}{dt} = k_{1f}c_O c_{N_2} + k_{2f}c_N c_{O_2} + k_{3f}c_N c_{OH} - k_{1b}c_{NO}c_N - k_{2b}c_{NO}c_O - k_{3b}c_{NO}c_H \tag{2.52}$$

The reaction rate coefficients $k_{1f}, k_{2f}, k_{3f}, k_{1b}, k_{2b}, k_{3b}$ for the forward reactions and corresponding backwards reactions can be expressed according to the Arrhenius law:

$$k = AT^{\beta} \exp\left(-\frac{E_{\beta}}{RT}\right) \tag{2.53}$$

where A is the pre-exponential factor, β indicates the order for the temperature dependence of the pre-exponential factor, E_{β} is the activation energy, T is the temperature and R is the universal gas constant. The concentration of O atoms and the free radical OH is calculated from empirical relations [30] based upon the radical concentration of the combustion model.

Under specific operating conditions, the rate of NO generated during the combustion of hydrocarbon fuel can be considerably higher than that predicted by the Zeldovich mechanism. This enhanced NO formation is attributed to the presence of hydrocarbon species, which result from fuel fragmentation during the combustion process. The prompt NO mechanism forms NO from nitrogen much earlier in the flame than the thermal NO mechanism, as its name suggest. Prompt NO becomes significant at low temperatures (below 800 °C), fuel-rich mixtures, and short residence time. It involves the intermediate formation of hydrogen cyanide (HCN), followed by the oxidation of HCN to NO. The following reactions are the most likely initiating steps from the prompt NO:

$$Fuel \rightarrow CH, CH_2 \ldots \tag{2.54}$$

$$CH + N_2 \leftrightarrow HCN + N \tag{2.55}$$

$$CH_2 + N_2 \rightarrow HCN + NH \tag{2.56}$$

The model used in this work to predict prompt NO concentration is calculated as:

$$\frac{dc_{NO}}{dt} = k c_{O_2}^{b} c_{N_2} c_{fuel} \exp\left(-\frac{E}{RT}\right) \tag{2.57}$$

where *c* denotes the concentration, *k* is the pre-exponential factor, *b* is the order of reaction for molecular oxygen and *E* is the activation energy.

The extended Zeldovich model can be coupled with ECFM-3Z+ combustion model based on equilibrium approach. While for the FGM method, the Zeldovich mechanism is incorporated in the chemical mechanism and is calculated during the pre-tabulation. The stored values of NO are then retrieved during the CFD simulation with FIRE.

3. Numerical setup

Numerical simulations were performed in the commercial three-dimensional (3D) CFD software AVL FIRE™. Within this chapter, the computational mesh is shown, along with the mesh dependency test. Afterwards, the boundary and initial conditions are provided including the spray setup. Finally, the simulation setup is given, providing the data on discretization schemes employed in this thesis along with convergence criteria and under relaxation factors.

3.1. Computational mesh

The moving computational mesh was generated using AVL™ ESE Diesel tool [15] based on the provided piston bowl geometry data. The experimental data of the direct injection diesel engine configuration are provided by AVL GmbH. The main specifications of the diesel engine are given in Table 1, while the generated meshes in the top dead centre (TDC) and bottom dead centre (BDC) are shown in Figure 4. The generated engine domain is only one-seventh of the total chamber with one nozzle since the combustion chamber geometry and the 7-hole injector configuration are cyclic symmetrical. A compensation volume is added to the original computational domain to get the correct compression ratio of the mesh and to compensate all inconsistency in the geometry of the cylinder head. The final mesh consists of hexahedral elements with the number of cells in the mesh 54 663 and 112 854 at TDC and BDC, respectively. A 2-cell thick boundary layer was created in the vicinity of wall selections declared in Figure 7 to capture the wall influence on the simulation results.

Table 1. Engine specification

Engine type	4-stroke DI diesel engine
Model	Volvo I5D
Number of cylinders	5, Inline
Displacement (cm^3)	2400
Bore (mm)	81
Stroke (mm)	93.15
Compression ratio	15.6

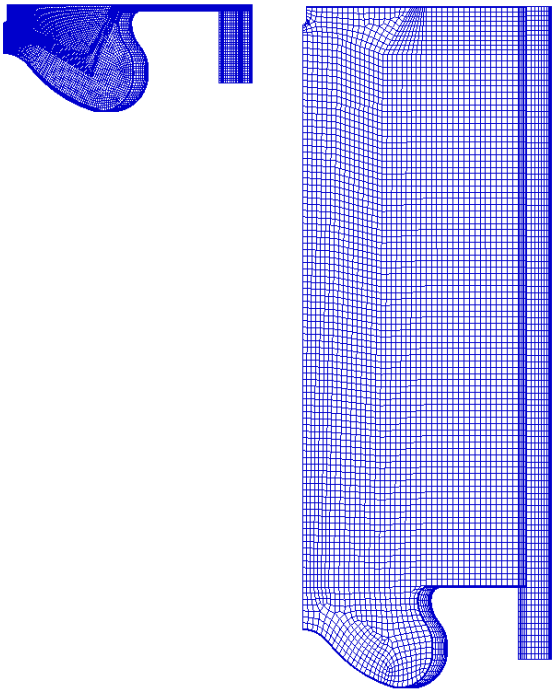

Figure 4. Generated computational mesh at TDC and BDC

3.2. Mesh dependency test

In every CFD simulation, it is essential to choose the discretisation level which provides the optimal choice between solution accuracy and computational time. The computational mesh should have a minimal number of cells which retains satisfying results. Therefore, a mesh study is performed. Three moving meshes with the same block structure, but with the different number of cells, were generated to test the impact of the mesh resolution on the simulation results, as shown in Figure 5. Characteristic data for each mesh is presented in Table 2. After the computational meshes were generated, the simulations with the same setup were run for all three meshes.

Table 2. Mesh dependency domain characterisation

Mesh resolution	Number of cells in TDC	Number of cells in BDC	Number of meshes
Coarse	54 663	112 854	35
Medium	73 542	112 854	35
Fine	109 473	112 854	35

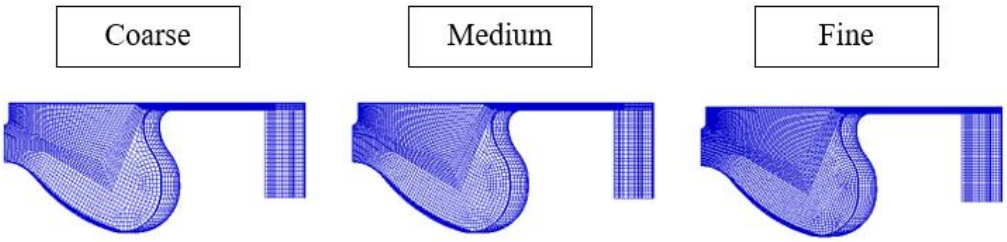

Figure 5. Computational meshes used for mesh dependency test

Figure 6 shows the comparison between calculated mean in-cylinder pressure and rate of heat release (RoHR) curves of individual domains with the experimental data. Only the period from the start of the fuel injection (718 °CA) to 750 °CA, is shown to gain better visibility of the results.

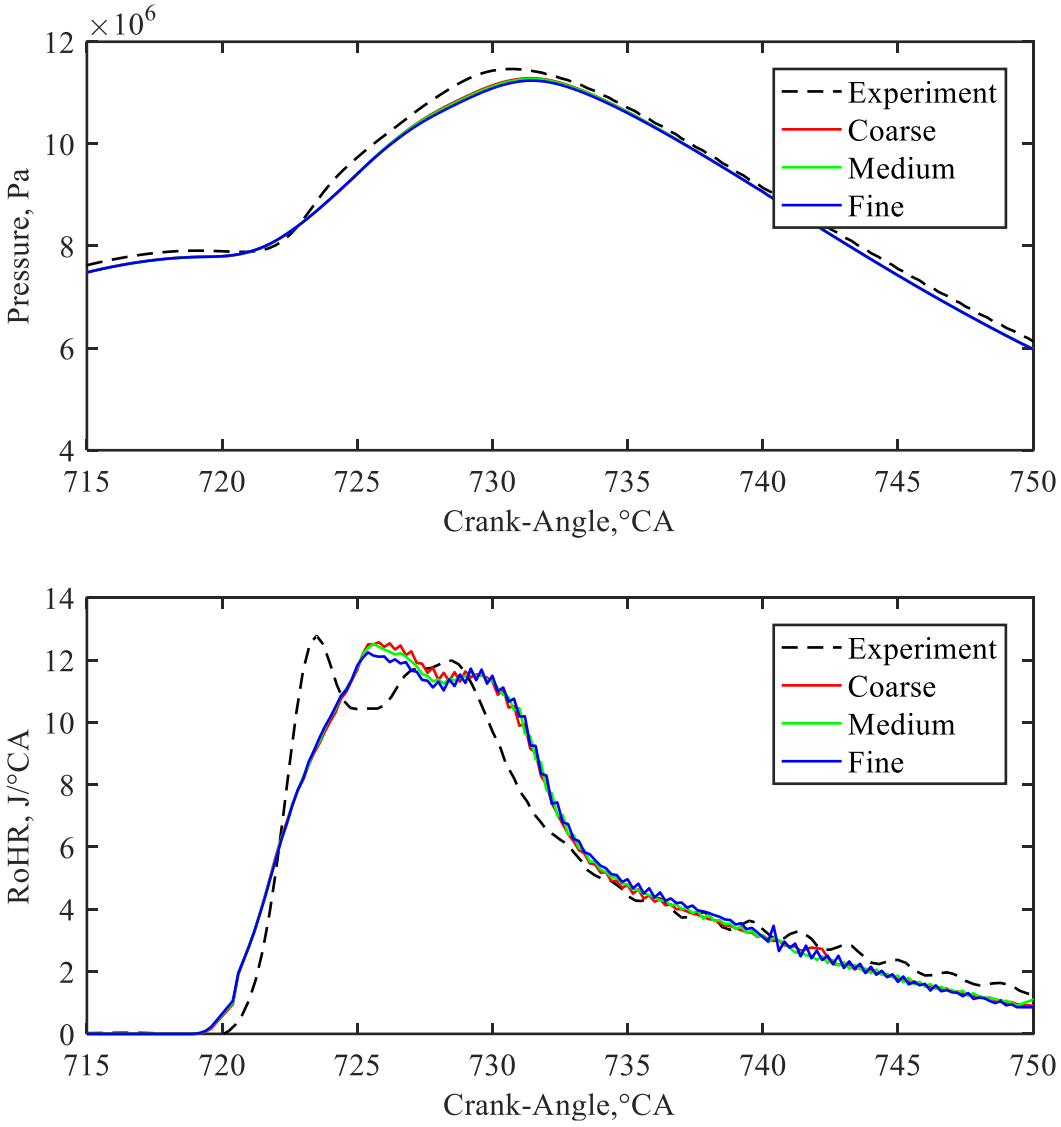

Figure 6. Mesh dependency of pressure and RoHR

Mesh dependency results exhibit similar values for all computational meshes. It can be concluded that the coarse mesh is able to provide satisfactory results. Hence it is used for all further calculations.

3.3. Boundary and initial conditions

To start numerical simulation corresponding boundary and initial conditions have to be defined on the computational domain. The boundary surfaces are defined through face selections displayed in Figure 7, while the defined boundary conditions are shown in Table 3.

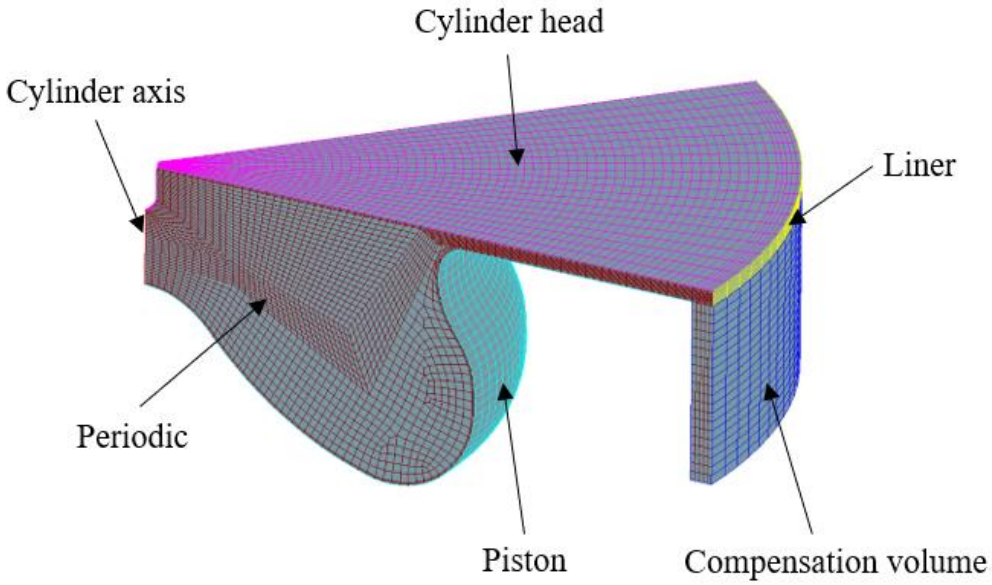

Figure 7. Boundary selections on the computational mesh

Table 3. Computational mesh boundary conditions

Selection	Boundary Type	Specific condition
Piston	Mesh movement	Temperature 473 K
Segment	Periodic inlet/outlet	Periodic
Cylinder Head	Wall	Temperature 443 K
Comp. Volume	Mesh movement/Wall	Adiabatic boundary
Cylinder Axis	Symmetry	-
Liner	Wall	Temperature 423 K

A moving, constant temperature wall boundary condition is applied to the piston surface, while the constant temperature condition is prescribed for the fixed cylinder head selection. A periodic boundary condition was applied to both sides of the mesh since the cylinder geometry was assumed to be symmetric around the cylinder axis. Furthermore, the compensation volume is assumed as an adiabatic boundary condition.

The initial pressure, temperature and gas composition were defined according to available experimental data. Initial conditions for four observed engine operating points are given in Table 4. The experiments were performed for the engine rotational speed 2000 min^{-1}. The initial velocity field inside the cylinder was defined with swirl value of 4740 min^{-1} around the cylinder axis. Case 1 and Case 2 represent operating points with single-injection strategy. In order to prove high predictability of the proposed modelling approaches, two cases with three injection pulses per cycle at the same rotation speed were observed, namely Case 3 and Case 4. Parameters such as the start and the end of injections together with corresponding injected fuel mass for all cases are shown in the following section.

Table 4. Initial conditions of the observed operating points

	Case 1	Case 2	Case 3	Case 4
Pressure (Pa)	219284	228547	210867	218474
Temperature (K)	427.2	388.6	418.9	365.4
Turbulent length scale (m)	0.002	0.002	0.002	0.002
Turbulent kinetic energy (m^2/s^2)	10	10	10	10

The initial gas composition inside the computational domain at the start of the simulation was defined as shown in Table 5, where Y_i represents the initial mass fraction of species.

Table 5. Initial values of species

	Case 1	Case 2	Case 3	Case 4
Y_{O2}	0.1855	0.2274	0.1830	0.2092
Y_{N2}	0.7579	0.7670	0.7580	0.7633
Y_{CO2}	0.0415	0.00413	0.04021	0.0187
Y_{H2O}	0.0151	0.00151	0.01880	0.0087

3.4. Spray setup

Properties of the liquid fuel used in performed simulations entitled as Diesel EN590 B7 are already available in FIRE™. The term B7 implies that there is up to 7% biodiesel content in the fuel [40]. The temperature of injected fuel was measured in the experimental research, and it is defined by 317.1 K. Employed spray submodels, described in Chapter 2 are given in Table 6.

Table 6. Spray submodels

Drag law mode	Schiller Naumann
Wall interaction model	Walljet1
Evaporation model	Abramzon – Sirignano
Breakup model	WAVE

The particle size at the fuel inlet is set to 125 μm. A number of introduced parcels per nozzle hole per time step equals the product of individual components in Table 7.

Table 7. Particle introduction from the nozzle

Number of different particle size introduced per time step and radius	3
Number of radial parcels release location on nozzle hole	6
Number of circular parcel release locations on each radial parcel	6

The main characteristic of the fuel injection system is shown in Table 8. The injector geometry required for simulation was taken over by the manufacturer. Spray angle delta 1 in Table 8 is the double angle between the spray axis and the nozzle axis.

Table 8. Injector geometry

Position	(0.5, 0, -1.5) mm
Direction	(0, 0, 1)
Spray angle delta 1	145
Nozzle diameter at hole centre position	1.84 mm
Nozzle hole diameter	0.125 mm

The Wave model constant C_2 was varied for both single-injection and multi-injection cases, with the three injection pulses being considered separately. Additionally, for all cases, Abramzon-Sirignano model constants E_1 and E_2 were varied. Furthermore, all constants were considered independently for two employed combustion models. In Table 9 and Table 10 are given applied values of spray model constants for single-injection and multi-injection cases for both combustion models, respectively, along with total injected fuel mass.

Table 9. Values of spray model constants for single-injection cases

	Case 1		Case 2	
	ECFM-3Z+	FGM	ECFM-3Z+	FGM
C2	5	20	19	5
E1	1	1	1.5	1
E2	1	0.9	1	2
Total mass (mg)	4.09		4.12	

Table 10. Values of spray model constants for multi-injection cases

	Case 3		Case 4	
	ECFM-3Z+	FGM	ECFM-3Z+	FGM
C2 for pilot and post injection	5	6	4	5
C2 for main injection	5	18	4	18
E1	1	1	2	1
E2	2	1	1	1
Total mass (mg)	3.95		3.95	

Figure 8 and Figure 9 show the injection rate for single-injection and multi-injection cases, respectively.

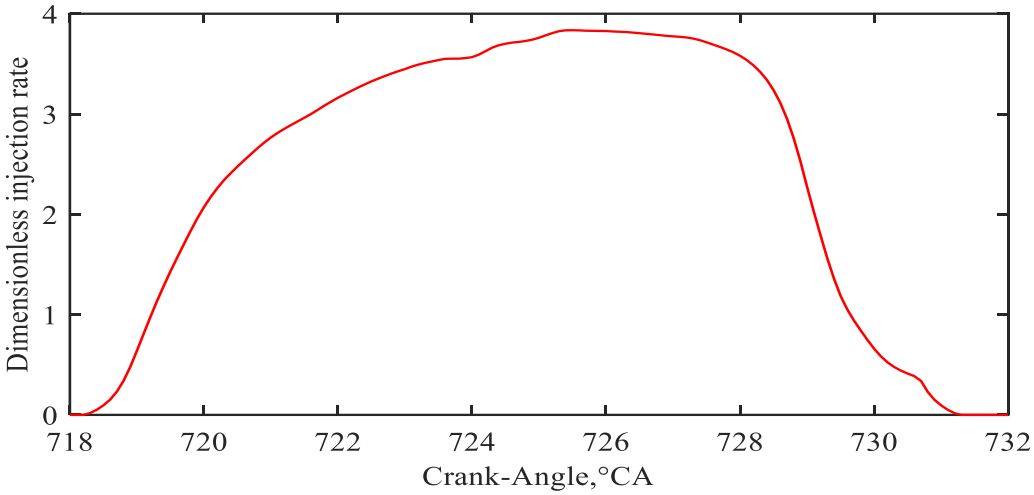

Figure 8. Injection rate for single injection cases

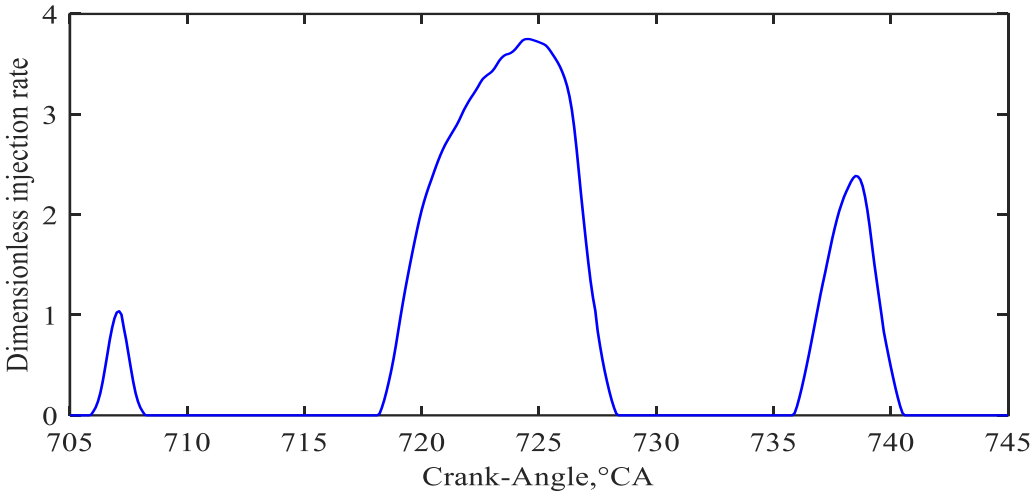

Figure 9. Injection rate for multi-injection cases

3.5. Combustion setup

When modelling combustion process with ECFM-3Z+ combustion model, some parameters have to be adjusted. In Table 11 are given applied values of model parameters. Mixing model parameter influences the fuel transfer from the pure fuel zone to the mixed zone. For modelling autoignition, Two-Stage model was employed. In this model, autoignition delay time is interpolated from pre-computed tabulated values. Inverse value of autoignition model parameter is multiplied with an ignition delay time from the databases, where the values larger than 1 are accelerating the ignition and vice versa. Chemical reaction time is set to 1 in all simulation cases. This value influences the rate of reaction of the fuel during the combustion process. Extinction temperature is set to recommended values.

Table 11. ECFM-3Z+ model parameters

	Case 1	Case 2	Case 3	Case 4
Mixing model parameter	2.2	0.9	1.5	0.8
Autoignition model parameter	Two-Stage	Two-Stage	Two-Stage	Two-Stage
Autoignition model parameter	4	2.3	1.2	4
Chemical reaction time (s)	1	1	1	1
Extinction temperature (K)	200	200	1500	1500

The FGM table generation tool contains three steps: pre-processing of textual input, PSR simulations, and post-processing of the output. The pre-processor translates the script into valid input for PSR solver and launches the individual simulations. The input data of a PSR table are summerised in Table 12, where pressure points are 40, 80, 120, 140, and temperauteres are selected in interval from 700 to 1800 K with the linear distribution. Mixture fraction grid is generated with 38 points where the refinement is around stoichiometric mixture fraction, 0.0450646. For genereation of PSR table a reduced reaction mechanism is used, namely LLNL Diesel reduced NOx, with 181 species and 1432 reactions [6].

Table 12. Input of PSR simulation

Input variable		Points
Z	Mixture fraction	38
S	Mixture fraction segregation	10
T	Temperature	12
p	Pressure	4

3.6. Solver setup

Transient, viscous and turbulent flow has been observed. The period of the numerical simulation was the same as the period of working cycle in the experimental data. The start of numerical simulation was set up to 585 °CA, and the end was defined at 855 °CA. In each operating point, the smallest time step size was used in the period where the injection and combustion process occurred. For the turbulence and energy transport equation, the first order upwind differencing scheme (UDS) was applied, while for the continuity equation, the central differencing scheme (CDS) was employed. The momentum equation was discretised using the MINMOD relaxed scheme, while the pressure – velocity coupling was performed using the SIMPLE algorithm [15].

The under relaxation factors determine a ratio between transported variable from previous and current iteration, and affects the convergence speed and stability of solver. As factor values approach zero, the solution stability increases, but the number of required iterations to achieve convergence is increased. As factor values approach 1, the solution stability decreases. The objective is to match each simulation with a set of under relaxation factors that balance the solution stability and the convergence rate to minimise the total processing time. Therefore, with the under relaxation factors, given in Table 13, the ratio of the solution in previous iteration entering in the new iteration is set.

Table 13. Under relaxation factors

Pressure	0.5
Momentum	0.6
TKE	0.4
TDS	0.4
Energy	0.95
Scalar	0.95
Species transport equation	0.95

Solving the non-linear partial differential equations comes down to the iterative procedure of the linearised system of equations until the solution reaches desired accuracy. After the normalised residuals fall below the set value, a numerical procedure for the following iteration is completed. The convergence criteria for performed calculations are given in Table 14.

Table 14. Convergence criteria

Maximum number of iterations	60
Minimum number of iterations	5
Pressure	10^{-5}
Momentum	10^{-4}
Energy	10^{-4}

4. Results

Within this chapter, the results of two 3D CFD combustion modelling approaches applied to the industrial diesel engine are shown. In the first section the combustion modelling results such as mean in-cylinder pressure, RoHR and mean temperature of single-injection operating points are compared with the experimental results. Secondly, the equivalent comparison is presented for two operating points with multi-injection strategy. Furthermore, the results for spray development and temperature field inside the engine combustion chamber for one multi-injection operating point are presented. Afterwards, the comparison of calculation times for different combustion modelling approaches is shown. Finally, the calculated NO_x emissions at the end of operating cycle are compared with the experimental data.

4.1. Single-injection results

The in-cylinder pressure results for Case 1 and Case 2 are shown in and Figure 10 and Figure 11, respectively. It is noticed that the FGM simulations in both cases underpredict the experimental pressure curve. Furthermore, numerical results of ECFM-3Z+ combustion model show better agreement during the entire time of simulation with the experimental results of mean in-cylinder pressure than the results with the FGM. Case 1 and Case 2 have the same injection timing and injection rate, but different initial oxygen concentration, which generates higher in-cylinder pressure in Case 2. The inflexion points visible around the TDC in both cases represent the start of the combustion. The pressure gradient increases due to the compression process until the evaporation of spray process during the pressure values are decreased. At the inflexion point, the heat from the chemical energy of the fuel is released, and the pressure gradient continues to rise to the maximum pressure. The inflexion points correspond to the initial declination of RoHR from the zero value as visible in and Figure 14 and Figure 15. However, from that point the pressure results obtained with the FGM model cannot be correlated with the presented RoHR results and mean temperature results shown in and Figure 12 and Figure 13.

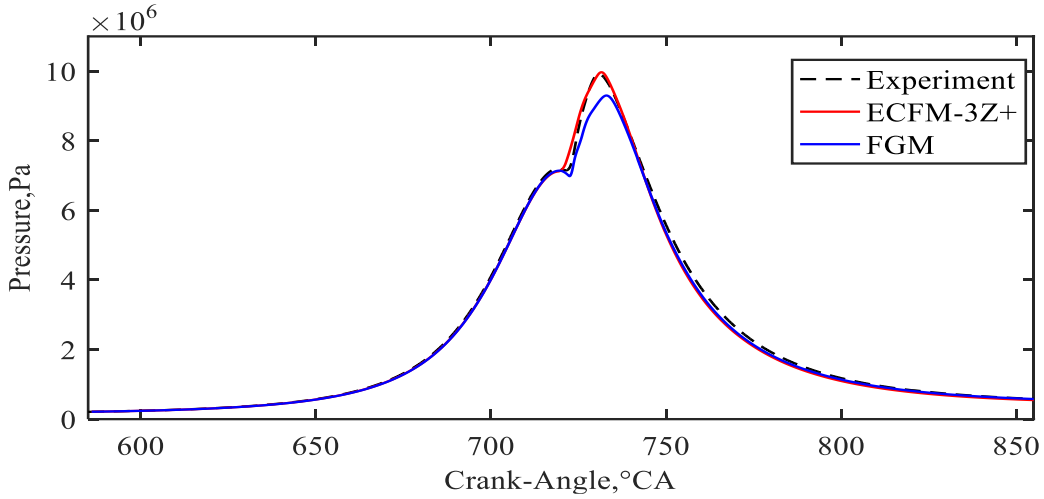

Figure 10. Mean pressure results for Case 1

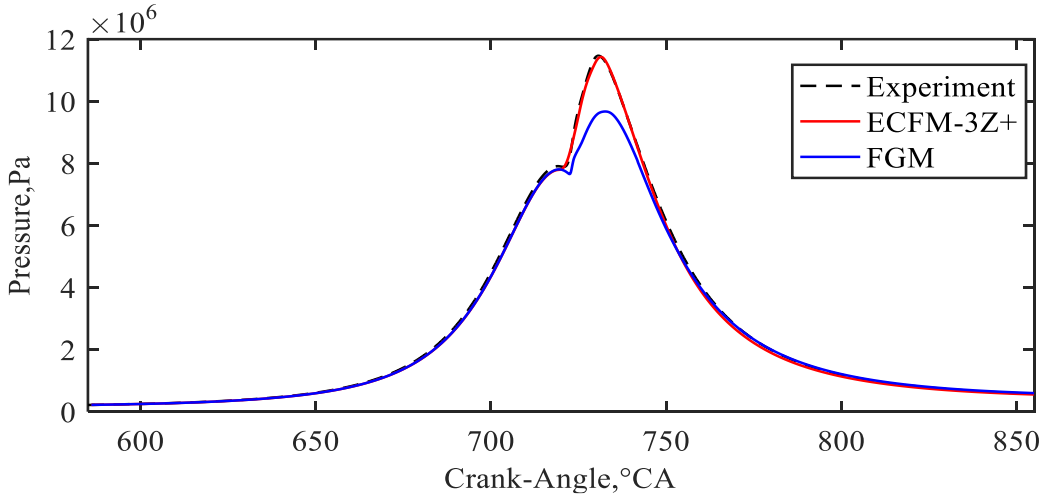

Figure 11. Mean pressure results for Case 2

Figure 12 and 15 show the differences in mean temperature curves obtained with the combustion models and experiment for Case 1 and Case 2, respectively. The differences in the pressure curves presented in Figure 10 and Figure 11 are also reflected in the temperature curves. The shape of the experimental curve is well captured with both combustion models in Case 1 as well as in Case 2. The FGM shows better prediction and agreement of peak temperature with the experimental data in Case 1, while the ECFM-Z+ shows better agreement in Case 2. Additionally, the FGM modelling approach shows a better prediction of the mean temperature with the experimental data in the late combustion phase than the ECFM-3Z+ model for both cases. In Figure 13, the ignition delay of FGM temperature is higher than in Case 1, which can also be seen from the RoHR curve in Figure 15. Such a pronounced ignition delay can be attributed to the lack of autoignition tuning parameter in the FGM model.

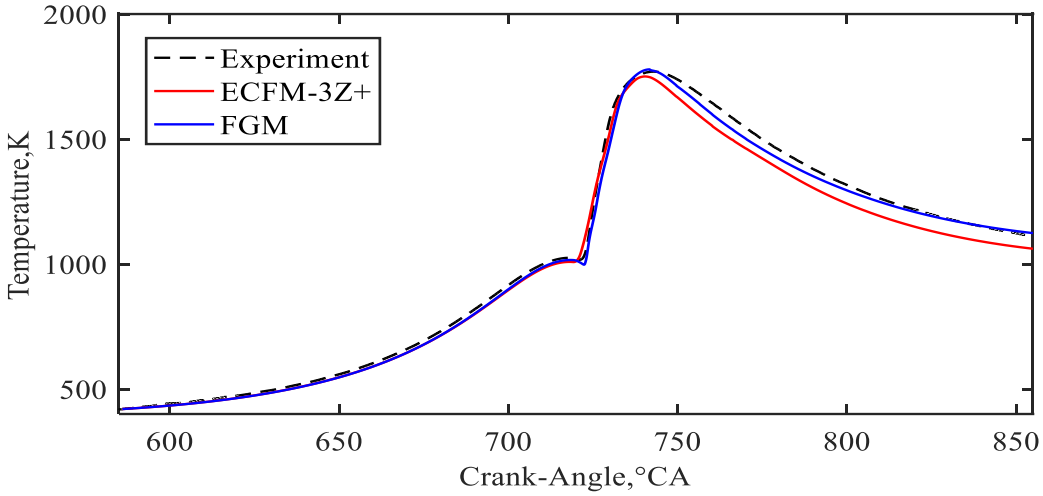

Figure 12. Mean temperature results for Case 1

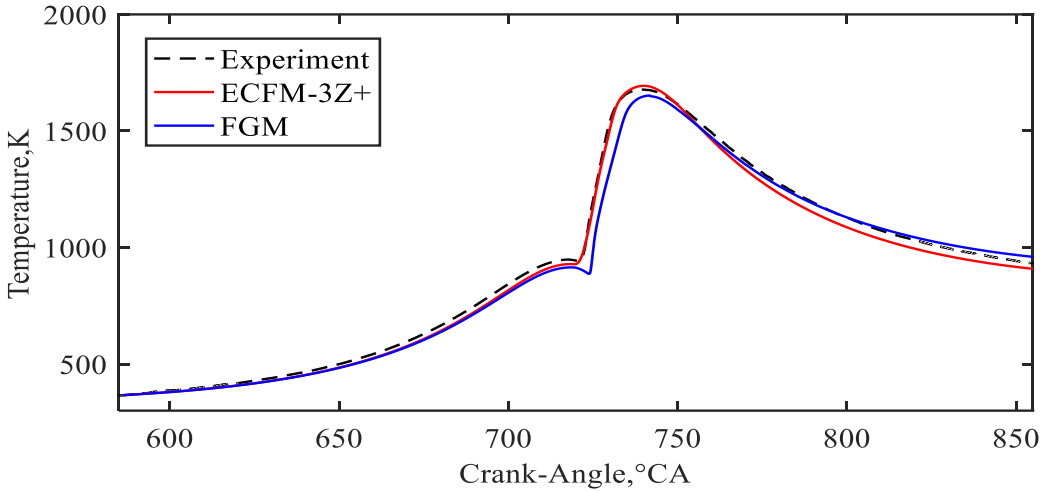

Figure 13. Mean temeprature results for Case 2

Figure 14 shows a comparison of the RoHR results obtained by the ECFM-3Z+ and FGM combustion approaches with the experimental data for Case 1, while Figure 15 shows comparison for Case 2. In Figure 14 and Figure 15, the showed RoHR curves are calculated for the one-seventh of the cylinder blow volume. This value should be multiplied by a number of nozzle holes and number of engine cylinders in order to obtain a value of RoHR for the entire engine. The start of the combustion or the autoignition point of fuel-air mixture corresponds to the initial increase of RoHR from the zero value. After start of the injection occurs, a specific delay is present due to mixing process before the start of the combustion, which is called ignition delay. It is notable from the presented results that the ECFM-3Z+ combustion model tends to predict the ignition earlier than the experimental data. On the contrary, the results obtained by the FGM combustion model show larger ignition delay. In

Case 1, the FGM combustion model predicts higher peak value of RoHR in comparison with the experiment, while the ECFM-3Z+ model predicts lower peek value of RoHR. While in Case 2, the peak values of RoHR are well predicted with both combustion models, although the result obtained with ECFM-3Z+ model has approximately 2 °CA offset in location. For both combustion modelling approaches, the RoHR profiles are in good agreement between Case 1 and Case 2. It can be noticed that the higher gradient of RoHR curve after the ignition exist in the FGM calculations, together with more pronounced local maximum values.

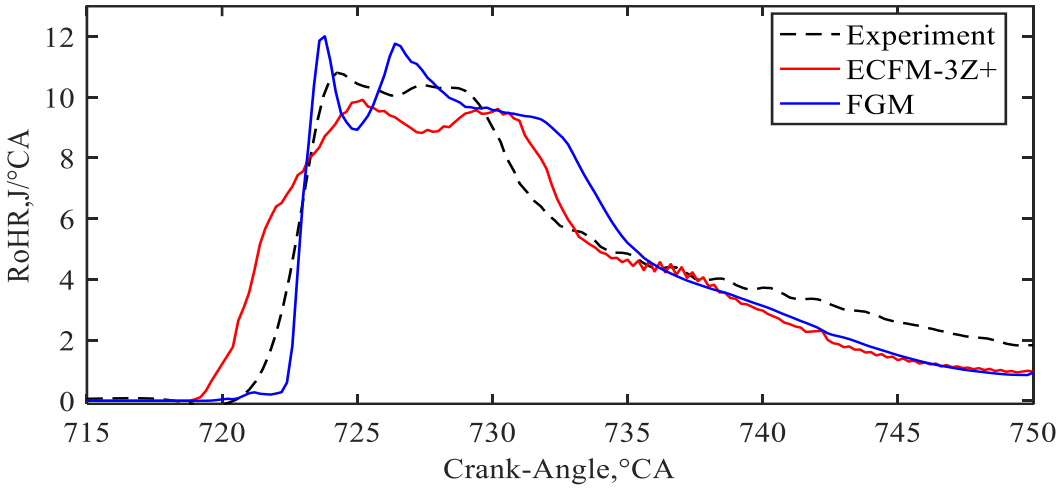

Figure 14. RoHR results for Case 1

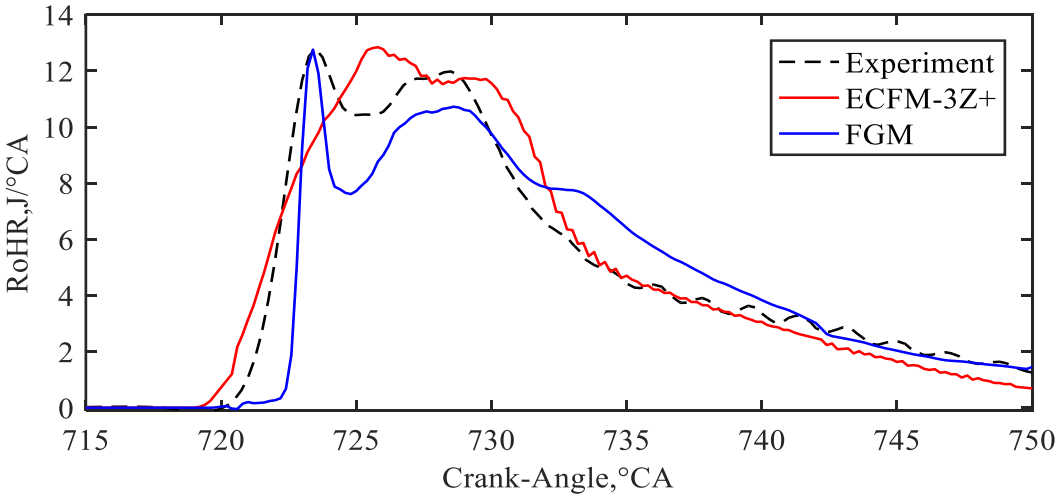

Figure 15. RoHR results for Case 2

4.2. Multi-injection results

Figure 16 and Figure 17 show the differences in mean pressure curves obtained with the combustion models and experiment for Case 3 and Case 4, respectively. In both cases, the results obtained with the FGM model show larger underprediction of the experimental curve than the results obtained with the ECFM-3Z+ model. That can be addressed to the smaller area under the calculated FGM RoHR curve than the area under the curve calculated with the ECFM-3Z+ model which are visible in Figure 20 and Figure 21. The higher-pressure values are reached in Case 4 than in Case 3, due to the higher initial oxygen concertation. The same underprediction of the peak pressure with FGM is achieved in the multi-injection operating points as in the single injection points shown in Figure 10 and Figure 11.

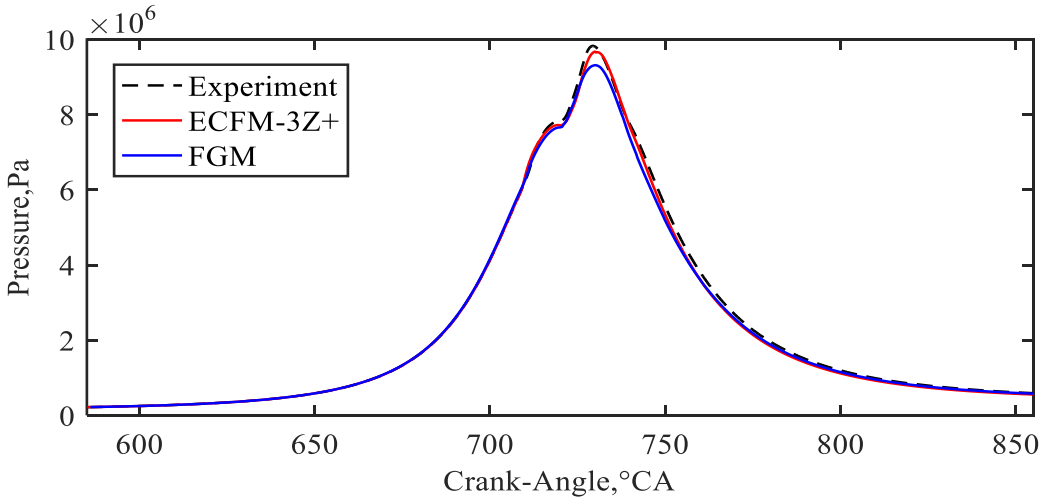

Figure 16. Mean pressure results for Case 3

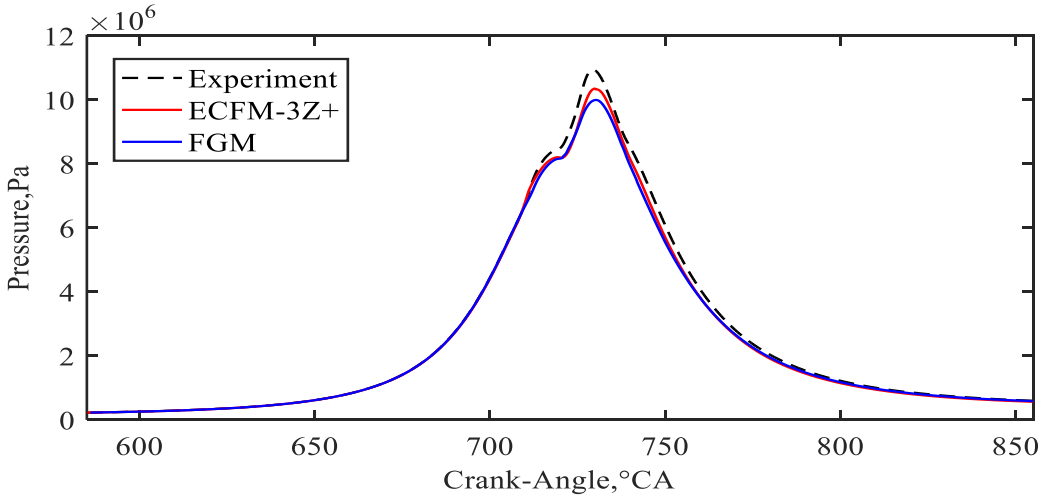

Figure 17. Mean pressure results for Case 4

Figure 18 and 19 show the differences in mean temperature curves obtained with the combustion models and experiment for Case 3 and Case 4, respectively. As well as for the single-injection operating points, the FGM modelling approach showed a better agreement of the mean temperature with the experimental data in late combustion phase than the ECFM-3Z+ model for both cases. The first inflexion point visible around the 705 °CA is the start of the combustion from pilot-injected fuel. The second inflexion point is around 720 °CA, and it corresponds to the ignition of the fuel injected in the main injection. The third inflexion point occurred when the ignition of the fuel injected in the post-injection start, and it is visible around the 735 °CA. Compared to the single-injection cases, in multi-injection cases lower peak temperatures are obtained, which can be addressed to the lower amount of injected fuel and broader RoHR curve during main injection shown in Figure 20 and Figure 21.

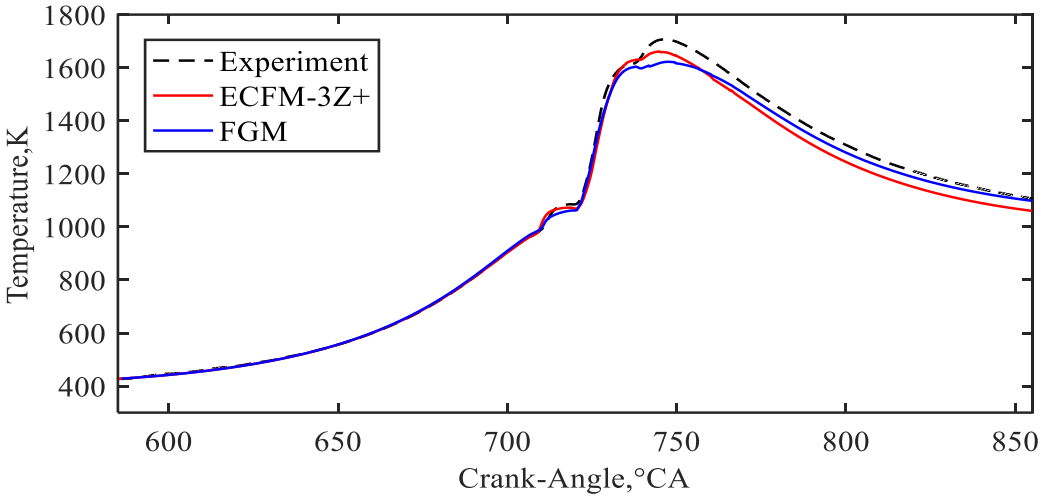

Figure 18. Mean temeprature results for Case 3

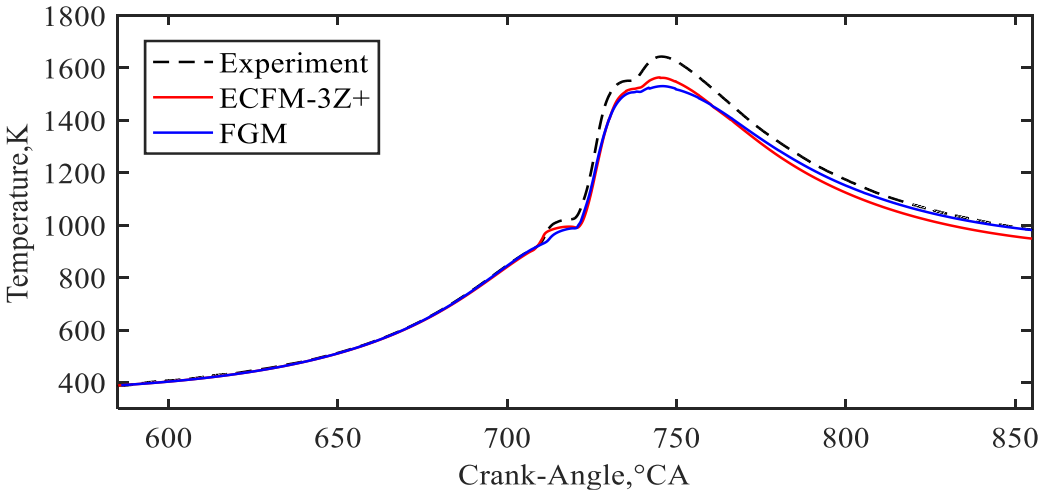

Figure 19. Mean temperature results for Case 4

Figure 20 shows the comparison of RoHR results obtained with the ECFM-3Z+ model and FGM model with the experimental data for Case 3. The area under the curves represents the accumulated energy, the energy realised from the fuel oxidation. The ignition of the fuel injected in the pilot injection predicted by the ECFM-3Z+ model is well captured, but the combustion of pilot injected fuel is faster than in experiment and FGM results. Also, the model overpredicts the peak value of the pilot heat release with ECFM-3Z+. The ignition of the fuel injected in post-injection is also well predicted, while the calculated RoHR curve underpredicts the experimental curve. Apart from that, the shape of the calculated RoHR curve fits well with the experimental data. Furthermore, the injection of the fuel injected in the main injection and the magnitude of heat release corresponds to the experimental data. The ignition of the fuel injected in the pilot injection predicted by the FGM model occurs slightly after recorded experimental data, and the peak value of the first heat release is underpredicted. In the part when the main and post-injection occur the RoHR curve obtained with the FGM exhibit the similar shape and magnitude as the one obtained with the ECFM-3Z+ model. In Figure 21, the differences between calculated RoHR results and the experimental data for Case 4 are shown. Notably, both calculated RoHR curves follow the same trend described in Case 3.

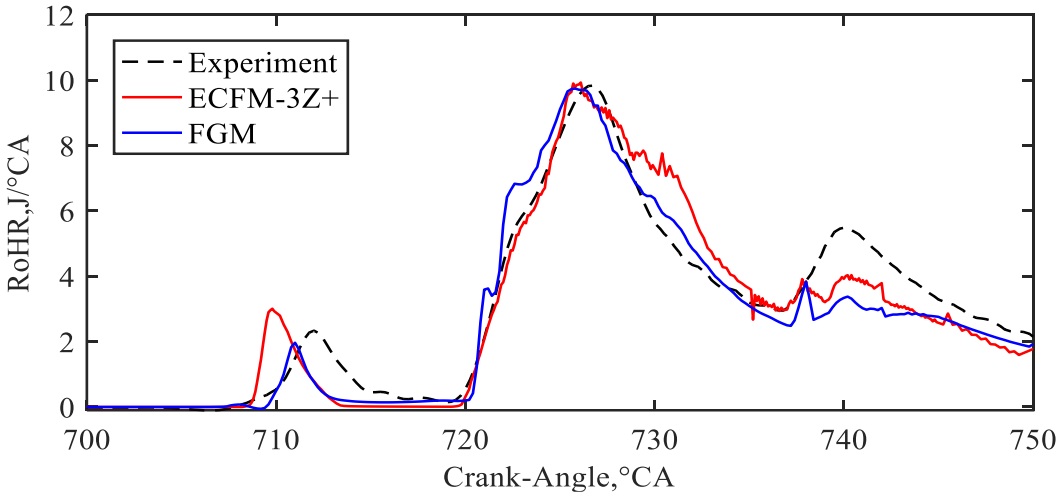

Figure 20. RoHR results for Case 3

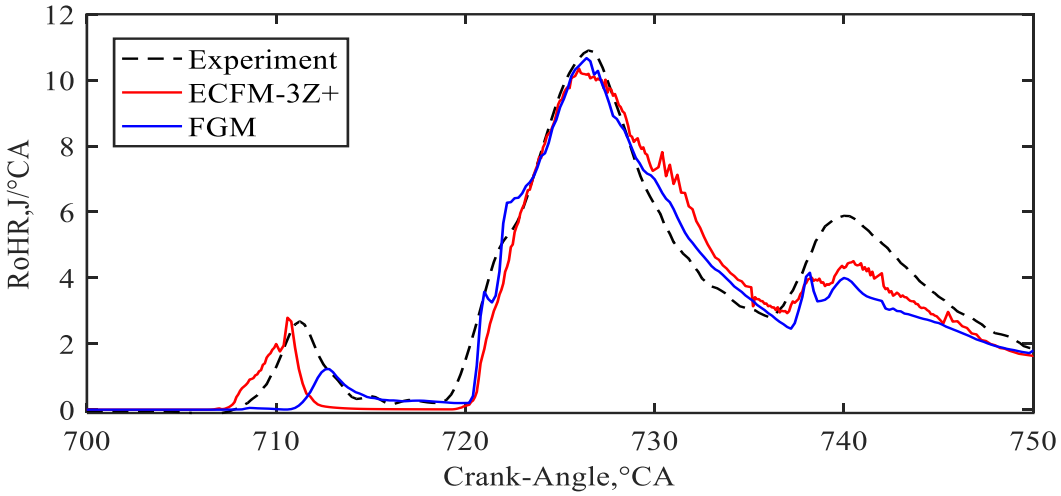

Figure 21. RoHR results for Case 4

With the application of the multiple injection strategies better control over the combustion process is achieved. Moreover, multi-injection strategy is effective in reducing not only the NO_x and PM but also diesel engine combustion noise.

In general, it can be stated, that both ECFM-3Z+ and FGM combustion modelling approaches are capable of predicting the combustion process in the real industrial diesel engines that feature multi-injection strategy.

4.3. Comparison of temperature fields

In Figure 22, the temperature field for different crank angle positions of Case 1 is shown. At the 718 °CA, few degrees before the TDC, liquid fuel is injected into the cylinder. The liquid fuel disintegrates into small diameter droplets and evaporates, which is visible into temperature reduction. After the fuel vapour is produced and mixed with the hot oxidising gas media in cylinder, ignition occurs, and in-cylinder pressure and temperature rise rapidly. It can be noticed that ECFM-3Z+ model shows a more intensive evaporation process, while the FGM spray region less spreader, due to the higher value of Wave breakup constant C_2. Such behaviour can be attributed to the faster ignition when comparing with the FGM model, that can also be seen in the ROHR curve in Figure 14. At 728 °CA and 740 °CA, it is visible that the ECFM-3Z+ model predicts broader high-temperature region characterised with the lower peak temperature, which is also visible in Figure 12. The peek temperatures are recorded at 740 °CA, where the maximum temperature is higher for the results obtained with the FGM

model. The temperature regions of both combustion modelling approaches are captured in good agreement during all operating cycle, where the main combustion exists in the cylinder bowl.

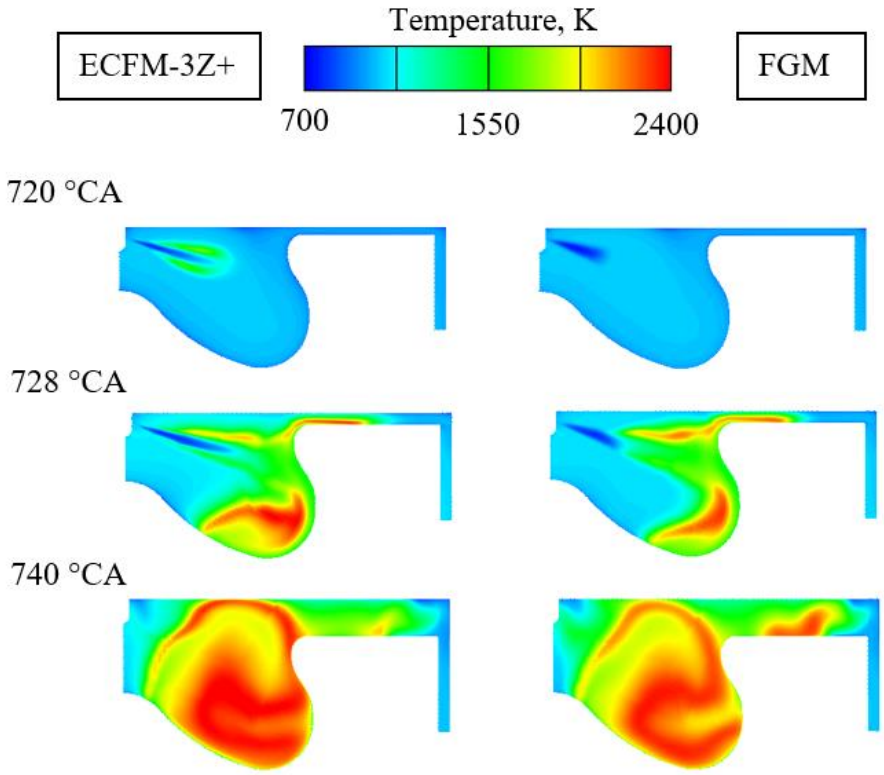

Figure 22. Temperature field for ECFM-3Z+ and FGM of the single-injection case

In Figure 23, the temperature field for different crank angle positions of Case 3 is shown. At 709 °CA, slightly after the pilot injection, the cooling of the gas phase is noticeable for the region where liquid fuel prevails. This phenomenon can be addressed to the lower fuel temperature and the evaporation process. At 721 °CA, the combustion of the vapour fuel from the pilot injection occurs, and the rise in temperature is visible in the combustion region. Additionally, it is visible, that ECFM-3Z+ predicts faster combustion of pilot-injected fuel. That can be addressed to the faster PI ignition visible in Figure 20. At the same crank angle, a lower temperature in the spray region is noticeable due to the evaporation process of the fuel from the main injection. If the multi-injection case is compared to the single-injection case in Figure 22, faster evaporation process is noticed. Such behaviour can be attributed to the higher in-cylinder temperatures achieved through pilot-injection combustion that further reduce the ignition delay of the main injection. Several degrees later, at 730 °CA, the combustion process of the fuel from the main injection has already started, and the high-temperature region is

formed. The post-injection occurs at 735 °CA, which is demonstrated with the lower temperature in the spray region. The maximum temperature is higher for the results obtained with the ECFM-3Z+ combustion model. It can also be observed in the temperature curve in Figure 18.

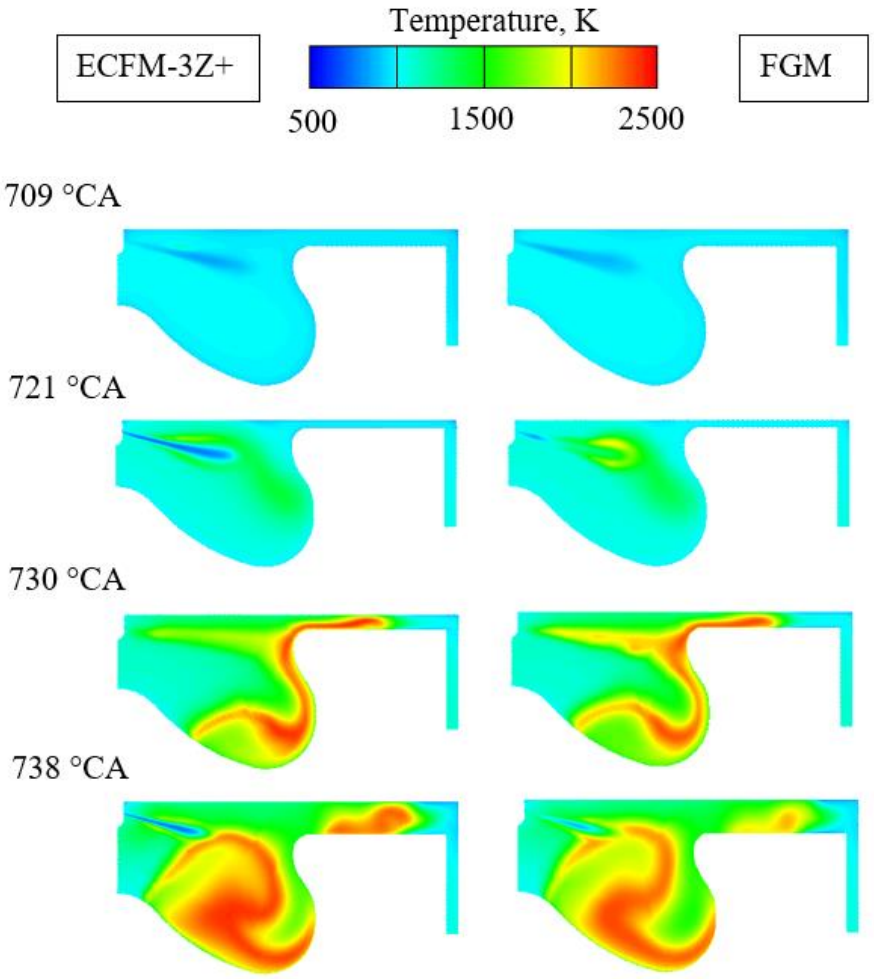

Figure 23. Temperature field for ECFM-3Z+ and FGM of the multi-injection case

4.4. Emissions results

The NO pollutant species are formed under high-temperature conditions within the flame region, where the NO formation is more pronounced at higher temperatures and the higher flame propagation rates. Among various types of vehicles, vehicles powered by compression ignition engines are one of the major contributors to the NO emissions. That is mostly consequence of their higher in-cylinder temperatures when compared to the gasoline engine. In the experimental research, the NO emission concentrations are measured in the exhaust pipe. In ECFM-3Z+ simulations, the NO formation was modelled using extended Zeldovich model. When using the FGM combustion model, all NO-related chemistry is computed during table generation according to the Zeldovich mechanism described in Chapter 2. Then, the stored values of NO are retrieved from the look-up tables during the CFD simulation as shown in Figure 2. Table 15 shows comparison of the calculated NO emissions with the experimental data for one single-injection operating point and one multi-injection operating point. As can be seen, the computed results with both combustion models are lower than the measured values of NO emission. Furthermore, in both cases the ECFM3-Z+ model showed higher values of NO emission in comparison with the FGM. That can be addressed to the higher prediction of the temperature presented in Figure 12 and Figure 18. As can be seen, the trend in the experimental NO reduction between Case 1 and Case 3 is well reproduced with both modelling approaches in CFD simulations. The calculated emission results indicate that both combustion models can perform the emission calculations with reasonable accuracy.

Table 15. NO mass fraction at the end of the operating cycle for Case 1 and Case 3

	Case 1	Case 3
Experiment (ppm)	135.6	119.1
ECFM-3Z+ (ppm)	133.02	83.7
FGM (ppm)	70.9	67.5

The comparisons between NO mass fraction distribution calculated using different combustion modelling approaches for Case 1 and Case 3 are shown in Figure 24 and Figure 25, respectively. For both combustion modelling approaches, the NO emissions are calculated from the mean quantities. The regions of NO can be examined by looking at contours of NO distribution and temperature field demonstrated in Figure 22 and Figure 23. It is noticeable that NO occurs wherever there is high temperature. At the 732 °CA, in both cases, a more

significant NO concentration can be seen in the region further away from the spray region. Furthermore, it is visible that in both cases ECFM-3Z+ results with the higher concentration of pollutant NO species due to a more progressive combustion process. At the later crank angle position, when high temperatures are achieved, both modelling cases exhibit a similar behaviour where the high-temperature regions are formed which ultimately leads to faster NO species formation. However, the ECFM-3Z+ model results with larger high-temperature region and thus with the wider NO mass fraction distribution in combustion chamber.

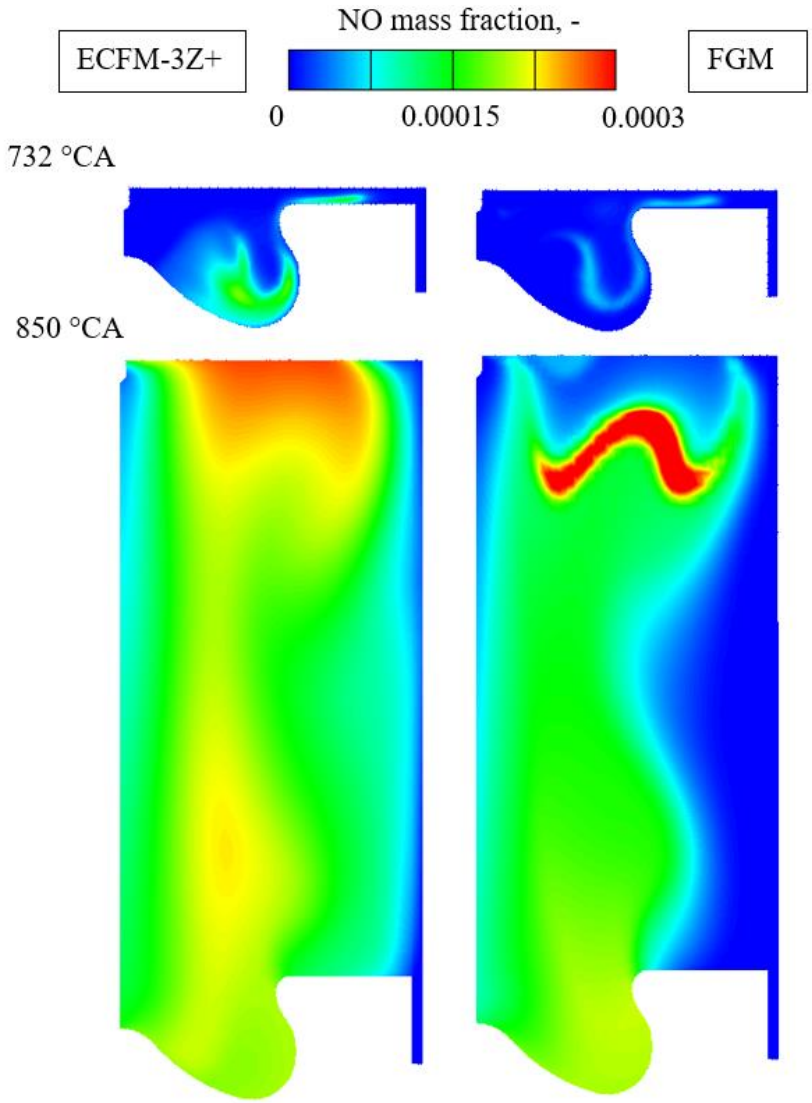

Figure 24. NO mass faction for Case 1

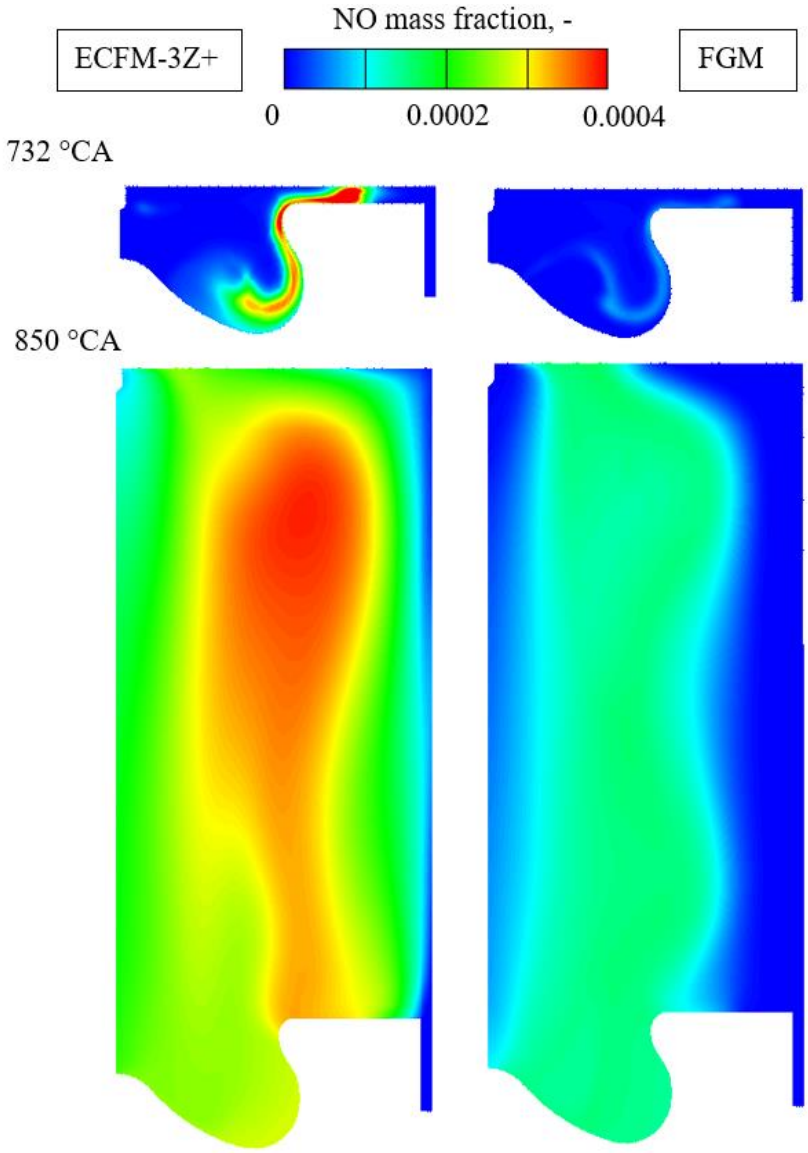

Figure 25. NO mass fraction for Case 3

4.5. Calculation time comparison

The FGM model allows including skeletal mechanisms as well as detailed reaction mechanisms in CFD simulations at a reasonable cost. Hence, the use of 3D CFD combustion models based on tabulated chemistry is becoming increasingly popular. In terms of computational time, the present study was executed on Intel® Xeon® E5-2650 processor, using four CPU cores per case. Comparison of the turnaround times for one single-injection and one multi-injection operating point is presented in Table 16. As can be seen from the table, reduction in the computational times is substantial – roughly two times.

Table 16. Comparison of calculation times for ECFM-3Z+ and FGM

	Case 1	Case 3
ECFM-3Z+ (hh:mm)	1:52	2:54
FGM (hh:mm)	0:42	1:18

5. Conclusion

In this thesis, the analysis of ECFM-3Z+ and FGM combustion modelling approaches coupled with experimental investigation of the diesel engine is performed. In order to prove high predictability of proposed modelling approaches, engine operating points with single-injection and multi-injection strategy are examined. The 3D CFD simulations were performed using commercial software AVL FIRE^{TM}, where the calculated results such as mean in-cylinder pressure, mean temperature and rate of heat release are compared to the experimental data, as well as calculated NO_x emissions.

It is shown, that the FGM modelling approach shows higher ignition delay compared to ECFM-3Z+ model for all single-injection cases, which can be attributed to the lack of the autoignition tuning parameters in FGM model. On the other hand, for the multi-injection cases both combustion approaches showed a good agreement with the recorded ignition time for pilot, main and post-injection. Furthermore, it is noticed, that the pressure results obtained with the FGM model exhibit under prediction of experimental pressure curve for all cases, while on the contrary presented RoHR and temperature curves fitting well with the experimental data. The FGM model showed a better prediction of the mean temperature with the experimental data in late combustion phase than the ECFM-3Z+ model for all cases. Moreover, the most significant impact on the result has Wave model constant C_2, which determines the droplet breakup time, and consequently the evaporation and combustion process. In the most ECFM-3Z+ simulations the C_2 constant was set to lower values compared to FGM spray setup thus the higher gradient of RoHR curve after the ignition exists in the FGM calculations. The trend in the experimental NO reduction between the observed cases is well reproduced with both modelling approaches in CFD simulations. The calculated emission results tend to be in a good agreement with the measured emission concentration indicating that both combustion approaches are capable of predicting the emissions in the real industrial diesel engines with reasonable accuracy. It should be noted that the runtime for CFD simulations with FGM is reduced roughly two times. Finally, it can be stated, that both ECFM-3Z+ and FGM combustion modelling approaches are capable of predicting the combustion process in the real industrial diesel engines since both approaches are validated against the experimental data for single and multi-injection strategy.

Bibliography

[1] FuelsEurope, 'Road fuel demand in the EU', 2019. [Online]. Available: https://www.fuelseurope.eu/wp-content/uploads/SR_FuelsEurope-2019-9.pdf.

[2] F. Jurić *et al.*, 'Experimental and numerical investigation of injection timing and rail pressure impact on combustion characteristics of a diesel engine', *Energy Convers. Manag.*, vol. 185, pp. 730–739, 2019.

[3] H. S. Chong, Y. Park, S. Kwon, and Y. Hong, 'Analysis of real driving gaseous emissions from light-duty diesel vehicles', *Transp. Res. Part D Transp. Environ.*, vol. 65, pp. 485–499, 2018.

[4] C. K. Westbrook, W. J. Pitz, O. Herbinet, H. J. Curran, and E. J. Silke, 'A comprehensive detailed chemical kinetic reaction mechanism for combustion of n-alkane hydrocarbons from n-octane to n-hexadecane', *Combust. Flame*, vol. 156, no. 1, pp. 181–199, 2009.

[5] M. Vujanovic, 'Lecture notes : Combustion and Radiation Modelling Course description ':, pp. 1–24.

[6] P. Gaffuri, C. K. Westbrook, H. J. Curran, and W. J. Pitz, 'A Comprehensive Modeling Study of n-Heptane Oxidation', *Combust. Flame*, pp. 1–37, 1997.

[7] N. Peters, 'Laminar flamelet concepts in turbulent combustion', *Symp. Combust.*, vol. 21, no. 1, pp. 1231–1250, Jan. 1988.

[8] O. Colin, A. Benkenida, and C. Angelberger, '3D modeling of mixing, ignition and combustion phenomena in highly stratified gasoline engines', *Oil Gas Sci. Technol.*, vol. 58, no. 1, pp. 47–62, 2003.

[9] O. Colin and A. Benkenida, 'The 3-zones Extended Coherent Flame Model (ECFM3Z) for computing premixed/diffusion combustion', *Oil Gas Sci. Technol.*, vol. 59, no. 6, pp. 593–609, 2004.

[10] F. A. Tap, R. Hilbert, D. Thévenin, and D. Veynante, 'A generalized flame surface density modelling approach for the auto-ignition of a turbulent non-premixed system', *Combust. Theory Model.*, vol. 8, no. 1, pp. 165–193, 2004.

[11] P. Béard, O. Colin, and M. Miche, 'Improved modelling of di diesel engines using sub-grid descriptions of spray and combustion', *SAE Tech. Pap.*, 2003.

[12] F. Catapano, M. Costa, G. Marseglia, P. Sementa, U. Sorge, and B. M. Vaglieco, 'Experimental and Numerical Investigation in a Turbocharged GDI Engine Under Knock Condition by Means of Conventional and Non-Conventional Methods', *SAE Int. J. Engines*, vol. 8, no. 2, pp. 437–446, 2015.

[13] J. Bohbot *et al.*, 'An Innovative Approach Combining Adaptive Mesh Refinement, the ECFM3Z Turbulent Combustion Model, and the TKI Tabulated Auto-Ignition Model for Diesel Engine CFD Simulations', *SAE Tech. Pap.*, 2016.

[14] R. Mobasheri, 'Analysis the ECFM-3Z Combustion Model for Simulating the Combustion Process and Emission Characteristics in a HSDI Diesel Engine', *Int. J. Spray Combust. Dyn.*, vol. 7, no. 4, pp. 353–371, Dec. 2015.

[15] 'AVL Fire Documentation'. 2018.

[16] S. H. Lam and D. A. Coussis, 'Understanding complex chemical kinetics with computational singular perturbation', *Symp. Combust.*, vol. 22, no. 1, pp. 931–941, 1989.

[17] U. Maas and S. B. Pope, 'Simplifying chemical kinetics: Intrinsic low-dimensional manifolds in composition space', *Combust. Flame*, vol. 88, no. 3–4, pp. 239–264, Mar. 1992.

[18] J. A. Van Oijen and L. P. H. De Goey, 'Modelling of Premixed Laminar Flames Using Flame-Generated Low-Dimensional Manifolds', *Combustion*, no. 2, pp. 2–5.

[19] A. Donini, R. J. M. Bastiaans, J. A. van Oijen, and L. P. H. de Goey, *A 5-D Implementation of FGM for the Large Eddy Simulation of a Stratified Swirled Flame with Heat Loss in a Gas Turbine Combustor*, vol. 98, no. 3. Flow, Turbulence and Combustion, 2017.

[20] C. Meijer and M. Tvrdojevic, 'Emissions predictions for Diesel engines based on chemistry tabulation', *Int. Multidimens. Engine Model. User's Gr. Meet.*, pp. 1–6, 2017.

[21] P. Priesching, M. Tvrdojevic, F. Tap, and C. Meijer, 'Prediction of the Combustion and Emission Processes in Diesel Engines Based on a Tabulated Chemistry Approach',

SAE Tech. Pap., no. April, pp. 18–21, Oct. 2017.

[22] D. Goryntsev, F. Tap, M. Tvrdojevic, and P. Priesching, 'SI engine combustion and knock modelling using detailed fuel surrogate models and tabulated chemistry', *SAE Tech. Pap.*, vol. 2019-April, no. April, pp. 1–14, 2019.

[23] C. Bekdemir, E. Rijk, B. Somers, P. De Goey, and B. Albrecht, 'On the application of the flamelet generated manifold (FGM) approach to the simulation of an igniting diesel spray', *SAE Tech. Pap.*, 2010.

[24] C. Meijer and R. O. G. Jr, 'Cfd Modelling of Partial Fuel Stratification Combustion Using', 2017, no. 3, pp. 1–8.

[25] A. D'Adamo *et al.*, 'Development of a RANS-Based Knock Model to Infer the Knock Probability in a Research Spark-Ignition Engine', *SAE Int. J. Engines*, vol. 10, no. 3, 2017.

[26] Z. Petranović, 'Numerical modelling of spray and combustion processes using the Euler Eulerian multiphase approach', *Digit. Proc. 2nd South East Eur. Conf. Sustain. Dev. Energy, Water Environ. Syst.*, p. 176, 2016.

[27] P. A. Durbin, 'Near-wall turbulence closure modeling without "damping functions"', *Theor. Comput. Fluid Dyn.*, vol. 3, no. 1, pp. 1–13, 1991.

[28] K. Hanjalić, M. Popovac, and M. Hadžiabdić, 'A robust near-wall elliptic-relaxation eddy-viscosity turbulence model for CFD', *Int. J. Heat Fluid Flow*, vol. 25, no. 6, pp. 1047–1051, 2004.

[29] A. Kadocsa, 'Modeling of Spray Formation in Diesel Engines', 2007.

[30] M. Vujanović, 'Numerical Modelling of Multiphase Flow in Combustion of Liquid Fuel', pp. 1–140, 2010.

[31] B. Jayashankara and V. Ganesan, 'Effect of fuel injection timing and intake pressure on the performance of a di diesel engine - A parametric study using CFD', *Energy Convers. Manag.*, vol. 51, no. 10, pp. 1835–1848, 2010.

[32] R. D. Reitz, 'Mechanisms of Atomization Processes in High-Pressure Vaporizing Sprays', *At. Spray Technol.*, vol. 3, pp. 309–337, 1987.

[33] AVL List GmbH, 'Avl fire ® version 2014.2', *Spray Modul.*, no. 08.0205.2014.2,

2016.

[34] W. A. Sirignano and B. Abramzon, 'Droplet vaporization model for spray combustion calculations', *Int. J. Heat Mass Transf.*, vol. 32, no. 9, pp. 1605–1618, 1989.

[35] J. A. Van Oijen and L. P. H. De Goey, 'Combustion Science and Technology Modelling of Premixed Laminar Flames using Flamelet- Generated Manifolds', *Combust. Sci. Technol.*, vol. 161, no. 1, pp. 113–137, 2000.

[36] F. Tap and P. Schapotschnikow, 'Efficient combustion modeling based on Tabkin® CFD look-up tables: A case study of a lifted diesel spray flame', *SAE Tech. Pap.*, 2012.

[37] Z. Petranović, T. Bešenić, M. Vujanović, and N. Duić, 'Modelling pollutant emissions in diesel engines, influence of biofuel on pollutant formation', *J. Environ. Manage.*, vol. 203, pp. 1038–1046, 2017.

[38] W. A. Majewski and M. K. Khair, *Diesel emissions and their control*. SAE International, 2006.

[39] J. B. Heywood, *IC Engine Fundamentals*, vol. 2010, no. 1. 1988.

[40] 'Diesel fuel Requirements , test methods and threshold values', 2009. [Online]. Available: https://www.ds-bremen.com/tl_files/media/pdf/eng_dieselkraftstoff_b7.pdf.